

UNIVERSITY OF CALGARY

The Shielding Effect of Polyethylene Coating Disbondment on Permeability of Cathodic  
Protection Current and the Resulting Pipeline Corrosion

by

Ke Yin

A THESIS

SUBMITTED TO THE FACULTY OF GRADUATE STUDIES  
IN PARTIAL FULFILMENT OF THE REQUIREMENTS FOR THE  
DEGREE OF MASTER OF SCIENCE

GRADUATE PROGRAM IN MECHANICAL ENGINEERING

CALGARY, ALBERTA

AUGUST, 2018

© Ke Yin 2018

## **Abstract**

The shielding effect of polyethylene (PE) coating disbondment on cathodic protection (CP) permeability was investigated. Results demonstrated that CP became shielded by disbonded PE coating. The geometrical factors of coating holiday (i.e., holiday size) and coating disbondment (i.e., disbonding width and depth) played an essential role in CP permeability. When sulfate-reducing bacteria (SRB) were contained in the thin layer of solution trapped under the disbonded PE coating, the corrosion of the steel depended heavily on the thickness of the solution layer. There existed a critical solution layer thickness, i.e., 150  $\mu\text{m}$ , where a maximum corrosion rate was reached. Pipeline corrosion in SRB-containing thin layers of solution trapped under disbonded coating was resulted from the synergism of microbiologically influenced corrosion (MIC) and the formation of corrosion product film on the steel surface.

## **Acknowledgements**

I would like to express my sincere gratitude to my supervisor, Dr. Frank Cheng for his constant guidance, encouragement, support and help throughout my whole master's program. His deep love and perception of science, his persistent endeavor for pursuing the truth, and his consistent efforts at achieving perfection have always inspired and helped me carry out this research project.

My sincere thanks also go to my committee members for serving as my examiners. Thanks to my group members, Dr. Hongwei Liu, Shan Qian, Yao Yang, Jialin Sun, and those whose names cannot all be listed here, for their helps and valuable discussions in this work.

The generous financial support from Enbridge Pipelines is highly appreciated and makes this work possible.

## **Dedication**

For

my beloved parents and other family relatives,  
and for others who have guided me over the past years.

## Table of Contents

Abstract .....	ii
Acknowledgements .....	iii
Dedication .....	iv
Table of Contents .....	v
List of Tables .....	vii
List of Figures and Illustrations .....	viii
List of Symbols, Abbreviations and Nomenclature .....	xi
CHAPTER ONE: INTRODUCTION .....	1
1.1 Research background .....	1
1.2 Research objectives .....	3
1.3 Contents of the thesis .....	4
CHAPTER TWO: LITERATURE REVIEW .....	5
2.1 Pipeline corrosion and corrosion control techniques .....	5
2.2 Polyethylene coating fundamentals .....	10
2.3 Coating failures and cathodic protection shielding .....	12
2.3.1 Coating failure mechanisms .....	12
2.3.2 CP shielding by defect-free, disbanded coating membranes .....	14
2.3.3 CP shielding at coating defects .....	15
2.3.4 CP shielding under disbanded coatings .....	16
2.4 Pipeline corrosion under coating disbondment .....	17
2.4.1 In the absence of microorganisms .....	17
2.4.2 In the presence of microorganisms .....	19
CHAPTER THREE: COMPATIBILITY OF POLYETHYLENE COATING WITH CATHODIC PROTECTION AND THE CORROSION OF CATHODICALLY PROTECTED PIPELINES UNDER DISBONDED COATING .....	23
3.1 Introduction .....	23
3.2 Experimental .....	24
3.2.1 Coating, steel and solution .....	24
3.2.2 Measurements of CP permeability of the PE coating .....	25
3.2.3 Surface characterization .....	28
3.3 Results .....	28
3.3.1 CP permeability of defect-free PE coating membranes with various thicknesses .....	28
3.3.2 CP permeability of PE coating containing a holiday with varied sizes .....	33
3.3.3 CP permeability at varied disbonding depths from the open holiday under PE coating disbondment .....	37
3.4 Discussion .....	45
3.4.1 Permeability of PE coating to CP .....	45
3.4.2 Effect of holiday size on CP permeability .....	46
3.4.3 Effect of the disbonding geometry on CP permeability under PE coating disbondment .....	48

3.4.4 Corrosion Mechanism of cathodically protected pipelines under coating disbondment.....	49
3.5 Summary.....	51
CHAPTER FOUR: MICROBIOLOGICALLY INFLUENCED CORROSION OF X52 PIPELINE STEEL IN THIN LAYERS OF SOLUTION CONTAINING SULFATE- REDUCING BACTERIA TRAPPED UNDER DISBONDED COATING .....	52
4.1 Introduction.....	52
4.2 Experimental.....	53
4.2.1 Material and solution.....	53
4.2.2 Experimental setup.....	54
4.2.3 Bacterial culturing and inoculation .....	55
4.2.4 Weight-loss measurements.....	56
4.2.5 Electrochemical measurements .....	57
4.2.6 Surface characterization .....	58
4.3 Results and discussion .....	58
4.3.1 Counts of sessile SRB cells on the specimen surface.....	58
4.3.2 Morphology of the surface films formed on the specimen.....	60
4.3.3 Compositional characterization of the surface films .....	62
4.3.4 Weight-loss measurements.....	64
4.3.5 Electrochemical measurements .....	65
4.3.6 Corrosion morphology of the steel specimen upon removal of surface film ..	72
4.3.7 Mechanistic aspects of pipeline corrosion and MIC in thin layers of sterile and SRB-containing simulated soil solutions trapped under coating .....	75
4.4 Summary.....	79
CHAPTER FIVE: CONCLUSIONS AND RECOMMENDATIONS.....	80
5.1 Conclusions.....	80
5.2 Recommendations.....	81
REFERENCES .....	82

## List of Tables

Table 3.1 Chemical composition of the extracted solution from Regina clay soil. ....	25
Table 3.2 Permeability of PE coatings with different thickness at the CP potential of -925 mV(CSE).....	46
Table 4.1 EDS results of the elemental composition of the surface films formed on the steel specimen after 15 days of testing under various solution layer thicknesses in the absence of SRB in the simulated soil solution. ....	63
Table 4.2 EDS results of the elemental composition of the surface films formed on the steel specimen after 15 days of testing under various solution layer thicknesses in the presence of SRB in the simulated soil solution. ....	63
Table 4.3 Fitted electrochemical corrosion parameters from the measured potentiodynamic polarization curves in Fig. 4.10.....	72

## List of Figures and Illustrations

Figure 2.1 The components of a typical corrosion cell.....	6
Figure 2.2 Coating developments since the 1940s.....	8
Figure 2.3 Schematic diagrams of (a) sacrificial anode CP system, and (b) impressed current CP system.....	9
Figure 2.4 Cathodic shielding problem in buried pipelines.....	14
Figure 2.5 Schematic illustration of EMIC and CMIC.....	21
Figure 3.1 Schematic diagram of the self-made test rigs to measure the CP permeability of (a) disbonded defect-free PE coating (with varied thicknesses), and (b) a disbonded PE coating (2.0 mm in thickness) with a holiday with varied sizes. ....	26
Figure 3.2 Schematic diagrams of the experimental setup to measure the CP permeability under disbonded PE coating in the simulated soil solution. ....	27
Figure 3.3 Optical views of the steel specimens after 30 days of testing in the simulated soil solution which is separated by a PE coating membrane with varied thicknesses (a – 0.0 mm b – 1.0 mm, c – 1.5 mm, d – 2.0 mm) in Fig. 3.1a, while a CP potential of -925 mV (CSE) is applied. ....	29
Figure 3.4 CP current densities measured on X52 steel electrode in the simulated soil solution separated by a PE coating membrane with varied thicknesses of (a) 1.0 mm, (b) 1.5 mm and (c) 2.0 mm under the CP potential of -925 mV (CSE). ....	30
Figure 3.5 Polarization current density of X52 steel at the applied CP potential of -925 mV (CSE) in the simulated soil solution. ....	31
Figure 3.6 Potential of the steel in the simulated soil solution separated by the PE coating membrane with varied thicknesses as a function time.....	32
Figure 3.7 pH of the soil solution which is separated by the PE coating membrane with varied thicknesses as a function of time at the applied CP potential of -925 mV (CSE). ....	33
Figure 3.8 Optical views of the steel specimens after 15 days of testing in the simulated soil solution separated by a PE coating membrane containing a holiday with varied sizes (a) 10 mm, (b) 4 mm, (c) 2 mm, (d) 1 mm, (e) 0.5 mm in Fig. 3.1b, while a CP potential of -925 mV (CSE) is applied at the holiday. ....	34
Figure 3.9 CP current density measured on the steel in the simulated soil solution separated by the PE coating containing a holiday with varied sizes at the CP potential of -925 mV (CSE) as a function of time.....	35

Figure 3.10 Potential of the steel in the soil solution separated by a PE coating containing a holiday with varied sizes at the CP potential of -925 mV (CSE) as a function of time.....	36
Figure 3.11 pH of the soil solution which is separated by the PE coating containing a holiday with varied sizes as a function of time at the applied CP potential of -925 mV (CSE).....	37
Figure 3.12 The morphology of the steel surface at varied disbonding depths (a) 0 mm, (b) 30 mm, (c) 60 mm, (d) 90 mm, (e) 120 mm, (f) 150 mm and (g) 180mm from the open defect (defect of 10 mm) under disbonded PE coating (disbonding thickness of 120 $\mu$ m) after testing for 15 days, where a CP potential of -925 mV (CSE) is applied at the holiday.....	38
Figure 3.13 The morphology of the steel surface at varied disbonding depths (a) 0 mm, (b) 30 mm, (c) 60 mm, (d) 90 mm, (e) 120 mm, (f) 150 mm and (g) 180mm from the open defect (defect of 10 mm) under disbonded PE coating (disbonding thickness of 240 $\mu$ m) after testing for 15 days, where a CP potential of -925 mV (CSE) is applied at the holiday.....	39
Figure 3.14 The morphology of the steel surface at varied disbonding depths (a) 0 mm, (b) 30 mm, (c) 60 mm, (d) 90 mm, (e) 120 mm, (f) 150 mm and (g) 180mm from the open defect (defect of 10 mm) under disbonded PE coating (disbonding thickness of 360 $\mu$ m) after testing for 15 days, where a CP potential of -925 mV (CSE) is applied at the holiday.....	40
Figure 3.15 Time dependence of cathodic current density of X52 steel under disbonded PE coating at varied disbonding depths from the open holiday (10 mm in diameter) with various disbonding thicknesses of (a) 120 $\mu$ m, (b) 240 $\mu$ m and (c) 360 $\mu$ m in the simulated soil solution, where a CP potential of -925 mV (CSE) is applied at the holiday.....	42
Figure 3.16 Time dependence of the distribution of local potential under disbonded PE coating at varied disbonding depths from the open holiday (10 mm in diameter) with various disbonding thicknesses of (a) 120 $\mu$ m, (b) 240 $\mu$ m, and (c) 360 $\mu$ m in the simulated soil solution, where a CP potential of -925 mV (CSE) is applied at the holiday.....	43
Figure 3.17 Time dependence of the distribution of solution pH under disbonded PE coating at varied disbonding depths from the open defect (10 mm in diameter) with various disbonding thicknesses of (a) 120 $\mu$ m, (b) 240 $\mu$ m and (c) 360 $\mu$ m in the simulated soil solution, where a CP potential of -925 mV (CSE) is applied at the holiday. ....	44
Figure 4.1 Schematic diagrams of the experimental setup of (a) top view of creating a disbonded PE coating on the steel specimen, where a thin layer of solution trapped in the disbonding crevice, and (b) front view of electrochemical measurements in the thin solution layer trapped under disbonded coating, where WE, RE and CE refer to working, reference and counter electrodes, respectively. ....	55

Figure 4.2 The counts of sessile SRB cells (i.e., $N_{\text{SRB}}$ ) attached on the specimen surface after 15 days of testing in the test solution with various thicknesses.....	59
Figure 4.3 SEM images of surface morphology of the steel specimens after 15 days of testing in (a) the sterile solution layer of 50 $\mu\text{m}$ in thickness and (b) the bulk solution, respectively. ....	60
Figure 4.4 SEM images of surface morphology of the steel specimen after 15 days of testing in the SRB-containing solution layers with various thicknesses (a) 50 $\mu\text{m}$ , (b) 150 $\mu\text{m}$ , (c) 400 $\mu\text{m}$ , (d) 1000 $\mu\text{m}$ , and (e) the bulk solution.....	61
Figure 4.5 Corrosion rate of the steel calculated from weight-loss measurements after 15 days of testing in the simulated soil solution with various thicknesses in the absence and presence of SRB, respectively. ....	65
Figure 4.6 Nyquist diagrams of the steel specimen measured in the (a) 50 $\mu\text{m}$ solution layer and (b) bulk solution in the absence of SRB as a function of time.....	66
Figure 4.7 Nyquist diagrams of the steel specimen measured in thin layers of solution with varied thicknesses and the bulk solution in the presence of SRB as a function of time (a) 50 $\mu\text{m}$ (b) 150 $\mu\text{m}$ (c) 400 $\mu\text{m}$ (d) 1000 $\mu\text{m}$ , (e) bulk solution. ....	67
Figure 4.8 Electrochemical equivalent circuits used to fit the EIS data measured in Figs. 4.6 and 4.7, where $R_s$ is solution resistance, $R_f$ and $Q_f$ are the resistance and constant-phase element of surface film, respectively, $R_{ct}$ and $Q_{dl}$ are charge-transfer resistance and the constant-phase element of the double-charge layer, respectively, and $W$ is Warburg element representing the diffusion process influenced by surface film.....	69
Figure 4.9 Time dependence of the fitted $R_p$ values from the measured EIS data in (a) Fig. 4.6 and (b) Fig. 4.7.....	70
Figure 4.10 Potentiodynamic polarization curves of the steel specimen after 15 days of testing in thin layers of solution and the bulk solution in the (a) presence and (b) absence of SRB, respectively. ....	71
Figure 4.11 SEM views of surface morphology of the steel specimens after 15 days of testing in the sterile (a) 50 $\mu\text{m}$ solution layer and (b) the bulk solution upon removal of the surface films.....	73
Figure 4.12 Corrosion morphology of the steel specimen after 15 days of testing in thin layers of solution with varied thicknesses in the presence of SRB upon removal of the surface films (a) 50 $\mu\text{m}$ , (b) 150 $\mu\text{m}$ , (c) 400 $\mu\text{m}$ , (d) 1000 $\mu\text{m}$ , (e) bulk solution. ....	74

## List of Symbols, Abbreviations and Nomenclature

Symbol	Definition
AC	Alternating Current
ASTM	American Society for Testing and Material
ATCC	American Type Culture Collection
CE	Counter Electrode
CEPA	Canadian Energy Pipeline Association
CMIC	Chemical Microbiologically Influenced Corrosion
CP	Cathodic Protection
CR	Corrosion Rate
CSA	Canadian Standards Association
CSE	Copper Sulfate Electrode
DC	Direct Current
EDS	Energy-Dispersive X-ray Spectrum
EIS	Electrochemical Impedance Spectroscopy
EMIC	Electrical Microbiologically Influenced Corrosion
EPS	Extracellular Polymeric Substance
FBE	Fusion Bonded Epoxy
GDP	Gross Domestic Product
HDPE	High-Density Polyethylene
HPCC	High-Performance Composite Coating
IOS	International Organisation for Standardization
LDPE	Low-Density Polyethylene
MDPE	Medium-Density Polyethylene
MIC	Microbiologically Influenced Corrosion
MPN	Most Probable Number
OCP	Open-Circuit Potential
PBS	Phosphate-Buffered Saline
PE	Polyethylene
RE	Reference Electrode
SCC	Stress Corrosion Cracking
SCE	Saturate Calomel Electrode
SEM	Scanning Electron Microscopy
SRB	Sulfate-Reducing Bacteria
UHMWPE	Ultra-High Molecular Weight Polyethylene
UV	Ultraviolet
WE	Working Electrode

## **Chapter One: Introduction**

### **1.1 Research background**

Pipelines are vital transportation arteries for the economy and specially for oil & gas industry. In Canada, a large and complex network of transmission pipelines covers more than 119,000 kilometers, delivering the energy people use every day, such as oil, gas and petroleum products [1]. According to Canadian Energy Pipeline Association (CEPA), operation of these energy transmission pipelines contributed \$11.5 billion to Canada's Gross Domestic Product (GDP) in 2015, and Alberta benefitted from nearly 44 percent of the total GDP impact [2].

Pipeline safety is a top priority for entire oil & gas industry. The integrity of the pipeline system can be severely threatened by a variety of factors, including corrosion, incorrect operation, weld/equipment failure, manufacturing/construction defects, cracking, excavation damage, etc. [3, 4]. Corrosion has been identified as the primary mechanism resulting in pipeline failures [5]. According to CEPA, corrosion is responsible for over 30 percent of the total pipeline incidents between 2010 and 2016 [2]. Specifically, the external pipeline corrosion accounts for more than 60 percent of total corrosion-induced pipeline failures, and becomes a major problem for these transmission pipeline systems [2, 6].

Pipeline systems are normally protected from external corrosion attacks by a combination of coatings and cathodic protection (CP). Coatings are the first line of defense, isolating the pipeline steel substrate from the corrosion environment, while CP serves as a back up to control corrosion if the external coating fails. As coating defect or disbondment develops a pathway for aggressive electrolytes to reach the pipe steel surface, the CP system should provide a further protection to the pipeline.

In reality, the supplemented CP does not always work effectively under a disbonded coating. The CP current can be fully or partially shielded from reaching the disbonded area when the coating disbonds at either small defects or a defect-free area [7-10]. As a result, the pipe steel still experiences corrosion in electrolyte even the CP is applied. Thus, disbondment of pipeline coatings is one of the most troublesome issues to maintain pipeline integrity [11]. Up to 85 percent of all external corrosion of cathodically protected pipelines occurs underneath the disbonded coatings that shield CP current [12, 13].

Polyethylene (PE) coating used to be the most commonly used pipeline coating and is still extensively used as the component of composite coatings. However, PE has been recognized as the one linking to the CP shielding issue [8, 14, 15]. Due to its high electrical strength, PE-based coatings are not expected to pass the CP current and thus shield the CP from reaching the pipe steel [13, 16]. Big efforts have been made to investigate the compatibility of PE coatings with CP against the pipeline corrosion under the coating disbondment. For example, Attar and Jalili [17] stated that the PE coating was sensitive to cathodic disbondment, and the disbondment usually took place in the primer layer. Margarit et al. [18] investigated the disbondment of the PE coating, and showed that the failure on the PE coating was more critical than on the non-shielding coating. In Cheng Laboratory at the University of Calgary, relevant works have been conducted in the past years. Fu and Cheng [19] found that medium-density PE (MDPE) coating is permeable to CP while the high-performance composite coating (HPCC) is impermeable to CP, and the impermeability of HPCC to CP is probably attributed to the modified adhesive layer contained in the coating. Howell and Cheng [20] shown that there is a quite small cathodic disbondment of HPCC under the standard test. Despite the research achievements, to date, a

thorough investigation of the CP shielding at various failure modes of PE coating has not been conducted.

In addition to the shielding effect on CP current permeation, the coating disbondment is also associated with a high degree microbiologically influenced corrosion (MIC) [21, 22]. Field investigations indicated that a larger number of sulfate-reducing bacteria (SRB) were counted at the corrosion sites under the disbonded coating than that in the bulk soil [23]. Once SRB participate in pipeline corrosion underneath the coating disbondment, the corrosion reaction kinetics accelerates significantly [24]. At the same time, the electrolytes trapped under the disbonded coating are usually thin. This is especially the case at the early stage of the disbondment where the steel corrosion experiences different processes, compared to that occurring in the bulk solution [25]. It is thus expected that corrosion, including MIC, of pipeline steel that occurs in a thin layer of electrolyte under the coating disbondment would have different mechanisms and rates from that in a bulk solution. However, there has been a limited understanding regarding the SRB induced pipeline MIC under disbonded PE coating, when CP is shielded. In addition, the effect of the solution layer thickness on pipeline MIC under the disbonded coating has remained unknown.

## **1.2 Research objectives**

The overall objective of this research is to advance the fundamental understanding of CP shielding under disbonded PE coating and pipeline MIC in the presence of SRB in the thin layer of electrolyte trapped under the disbondment. Progress has been made in the following two areas:

- 1) To study the geometric effects of PE coating disbondment on CP shielding; and to understand the pipeline corrosion under disbonded PE coating.
- 2) To investigate the mechanistic aspects of SRB-induced MIC on pipelines in thin layers of solution trapped under disbonded PE coating; and to characterize the effect of the solution layer thickness on pipeline MIC.

### **1.3 Contents of the thesis**

This thesis contains six chapters. Chapter One gives an overall introduction of the background to the research, together with the research objectives.

Chapter Two reviews the basic facts related to this research, including an overview of pipeline corrosion and corrosion control techniques, fundamentals of PE-based pipeline coatings, principles of coating failures and the resulting CP shielding, and the understanding of pipeline corrosion under coating disbondment in the absence and presence of microorganisms.

Chapter Three investigates the shielding effect of PE coating on CP at various coating failure modes and the corrosion of an X52 pipeline steel under the disbonded PE coating in a simulated soil solution. The parametric effects on the CP permeability and pipeline corrosion are determined.

Chapter Four studies the MIC of X52 pipeline steel in thin layers of simulated soil solution in the presence of SRB under the disbonded PE coating. The effect of solution layer thickness on the steel corrosion is determined and the mechanism of pipeline MIC in thin layers of solution under disbonded PE coating is discussed.

Chapter Five concludes the research and provides recommendations for the further work.

## Chapter Two: Literature Review

### 2.1 Pipeline corrosion and corrosion control techniques

Corrosion is a natural degradation of engineering materials, causing over 50 percent failures of global pipeline system and costing the industry trillions of dollars annually [26]. Pipeline corrosion can be defined as the deterioration of pipe material due to electrochemical reactions with the service environment [1, 27]. Uncontrolled pipeline corrosion can lead to either leaks or ruptures. Leaks are more common and can contaminate the surrounding soils and water. Ruptures are more likely to cause an explosion and fire, thus resulting in more disasters and injuries.

The fundamental of corrosion is the formation of a corrosion cell which is comprised of the following three essential components (**Fig. 2.1**):

**Anode:** It is the area where corrosion occurs. The reactions take place here are oxidation reactions. For pipeline steels, the anodic reaction is the iron dissolution:



**Cathode:** It is the area where reduction reactions occurs, where electrons released by the anodic reactions are consumed at the cathode surface. The specific cathodic reaction depends on the nature of the electrolyte:





**Electrolyte:** It is the electrically conductive solution for ionic movement, which must be present for corrosion to occur.

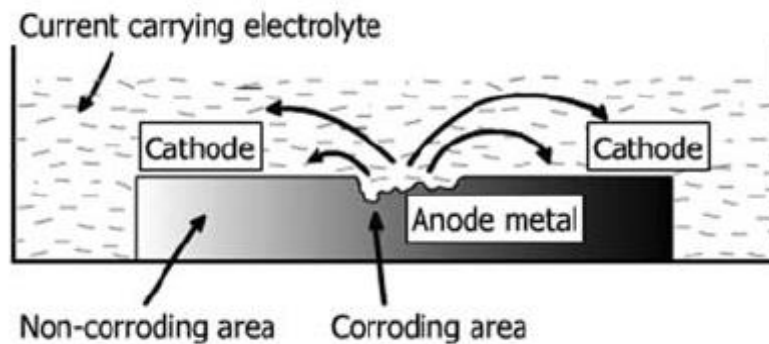


**Figure 2.1** The components of a typical corrosion cell [28].

Pipeline corrosion is specific both to the material and the environmental interactions [5]. Because of the different combinations of materials and service environments, a wide variety types of corrosion are encountered in oil & gas pipelines, such as uniform corrosion, galvanic corrosion, pitting corrosion, stress corrosion cracking (SCC), MIC, etc. Transmission pipelines are made of steels, especially carbon steels, and buried underground. Their service environment would be groundwater or wet soil. Since pipelines are always exposed to underground soil environment, the external corrosion is expected to occur on pipelines. Therefore, unprotected pipelines will deteriorate over time and eventually fail. In the case of pipelines that carry flammable, explosive and potentially contaminating substances, the safety and structural

integrity of pipelines are paramount. Hence, the corrosion control has long been considered an extremely important issue for the oil & gas industry [29].

Nowadays, different techniques exist to control pipeline corrosion and extend pipeline service life. The primary method of preventing or mitigation external corrosion of buried pipelines involves a combination of coatings and CP. Applying a protective coating is one of the most effective ways to protect pipelines from corrosion. It is the first line of defense against corrosion in pipeline systems. An intact and well-adhered coating directly separates the pipeline from the service environment that causes corrosion. Over the past few decades, the technology surrounding pipeline coatings has continuously been improved, and a wide variety of new coatings has been developed to improve the integrity of oil & gas pipelines. The development of pipeline coatings since the 1940s is shown chronologically in **Fig. 2.2**. Polymeric coating systems have a finite life and would degrade with time, eventually allowing oxygen, water, and chemicals to reach the substrate. Moreover, coating damages during various stages of pipeline design, transportation, construction and operation are inevitable [30]. Therefore, coatings by themselves would not be effective for pipeline protection. Hence, CP is required to continue prevent pipelines from corrosion attack as coating fails.

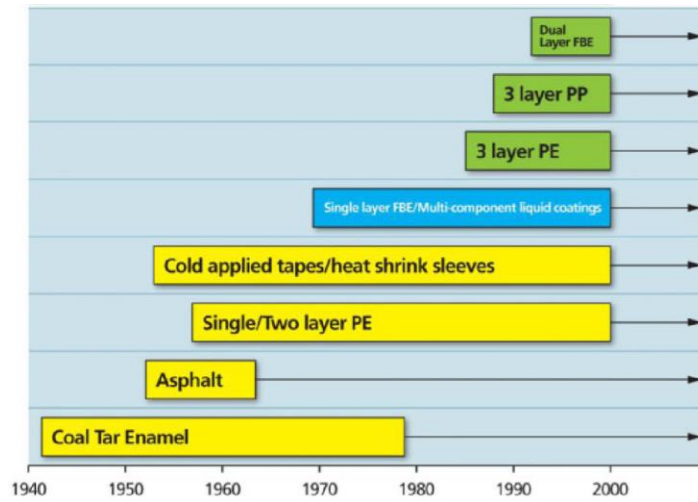


**Figure 2.2 Coating developments since the 1940s [15].**

CP is an electrochemical method of corrosion control by making the pipeline as the cathode of an electrochemical cell. It involves applying a current on the pipeline through soil from an external power supply. The pipe steel is polarized cathodically to override corrosion-induced anodic current under damaged coating. Thus, the exposed pipeline (anode) can be made to behave like a cathode. The principle of CP consists of reducing the corrosion potential of the steel structure, bringing the steel close to an immune state and controlling its corrosion rate. At the same time, an alkaline environment is usually produced at the pipe surface accompanying with the CP application. In many soils, calcareous deposits (a layer containing mixture of calcium carbonate and magnesium hydroxide) will form on the steel surface in this alkaline environment and further protect the steel. CP could be achieved either by sacrificial anodes or by an impressed current system, as illustrated in **Fig. 2.3**. In sacrificial anode cathodic protection systems, the source of cathodic current for negative polarization of the steel structure is supplied by the dissolution of a more active metal (spontaneously anodic to the protected structure).

Electrons flow from the more active electrode (anode) placed in the environment to the pipeline structure (cathode) due to the difference in the electrical potential. This technique is typically used in high conductive environments, such as seawater, and when a low protection current is required. Alloys of zinc and magnesium are the sacrificial metals most commonly employed to protect pipeline steel. In contrast to sacrificial anode system, the cathodic polarization of the structure is provided by an external direct current (DC) power supply (rectifier) in impressed current cathodic protection systems. The protective current is distributed by specially designed inert anodes, generally a conductive material which is not consumed during service. This system is usually adopted in high resistive environments, generally soils and concrete, and are preferred when protecting extended structures due to the higher flexibility in the current supply. In practice, the impressed current system is more economical and effective to mitigate corrosion of long-distance buried pipelines due to its flexible voltage and current outputs and a longer service life.

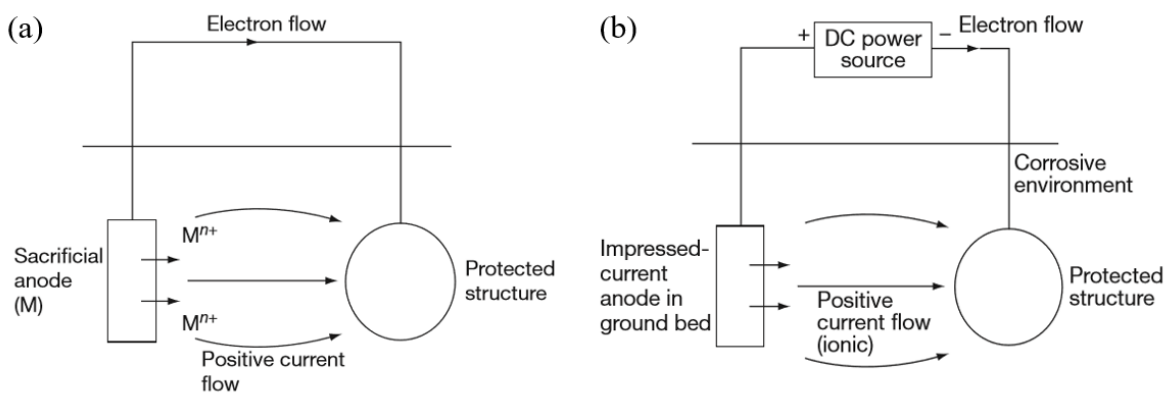


**Figure 2.3 Schematic diagrams of (a) sacrificial anode CP system, and (b) impressed current CP system [31].**

CP current is very effective when it has a path to flow to the pipe steel. However, when coating disbondment or blistering occurs, some types of coating can shield CP current from its intended path to that part of the pipe. Therefore, CP current cannot adequately protect the external surfaces of pipe, and corrosion will continue unless the coatings are replaced. Most external corrosion on pipelines is caused by disbonded coatings that shield CP, not lack of CP. PE-based coating is typically one to shield CP.

## **2.2 Polyethylene coating fundamentals**

PE, a thermoplastic polymer, is a semi-crystalline material with an excellent resistance to water, chemicals, wear and impact. It has a high electrical strength and water resistance, both of which are unaffected by humidity and temperature in the normal service conditions [30]. PE is formed by polymerization of ethylene (i.e.,  $\text{CH}_2=\text{CH}_2$ ). Based on the polymerization process, PE can be classified by low-density PE (LDPE), MDPE, high-density PE (HDPE) and ultra-high molecular weight PE (UHMWPE), in accordance with its structure (density and branching) and molecular weight [32]. The properties of PE depend largely on its structure and molecular weight. For example, with an increase in density, the level of branching decreases, and PE has stronger intermolecular forces and tensile strength.

PE is the foundation for many pipeline coatings and was first introduced in the 1950s. Since then, PE-based coatings have increased in use due to their excellent resistance, easy handling, nontoxicity, and the lower environmental impact. At present, they are used extensively in the oil & gas industry. PE-based coatings have been developed from single- and two-layer systems to three-layer and composite coating systems.

**PE tapes:** This coating system consists of a PE layer backed with a rubber adhesive in a tape form. The adhesive layer is mainly composed of butyl rubber along with additives that aim to facilitate excellent adhesion to pipe steel surface as well as a good bonding with the outer layer [33]. The outside layer is the mechanical layer, made of PE. It is usually resistant to ultraviolet (UV) light for above-ground storage. This system can be used in a wide variety of sizes, thicknesses, and compositions, making it a versatile corrosion-resistant coating. However, PE tapes are declining in use because of poor adhesion (causing coating disbondment), and the associated external corrosion and SCC occurrence. Nowadays, PE tapes are primarily used on small-diameter pipelines for areas of field repair [34].

**Dual-layer PE coatings:** Introduced in the 1960s, this type of coating was formulated to resist most biological, chemical and environmental contaminants found in the soil. It is comprised of a continuous outer layer of HDPE extruded over a rubber modified asphalt base. The dual-layer PE coating, widely known as “Yellow Jacket” because of its characterized color, is ideal for protecting distribution pipeline systems and small-diameter transmission pipelines in oil & gas industry.

**Three-layer PE coatings:** This coating system, developed in the early 1980s, intended to combine the superior adhesion and cathodic disbondment resistance of fusion bonded epoxy (FBE) with the high mechanical strength of PE. It consists of an FBE primer, a copolymer adhesive layer, and either an extruded or a wrapped outer layer of PE. Generally, the system with a wrapped outer layer has a better coating performance than the one with an extruded outer layer [30]. The main problems of the three-layer PE coatings are stress cracking of the outer layer of PE, increased susceptibility to AC and DC stray current induced corrosion in areas of coating damage, and the loss of adhesion to pipe steel surface [35]. The coating disbondment, subjected

to service conditions of buried pipelines, can involve numbers of chemical, physical, and mixed reactions that lead to pipeline failures. The coating disbondment is most probably attributed to degradation of the FBE layer or poor surface preparation of the steel substrate [36].

**Multi-component single-layer PE coatings:** Multi-component single-layer PE coating system was first designed in 1992, and is now widely considered as an effective protection for maintaining the integrity of pipeline systems, especially in harsh, extreme weather environment like the Arctic regions. This coating is commonly known as HPCC, and consists of an FBE primer, a MDPE out layer, and a tie layer containing a chemically modified PE adhesive. These three components are blended together to minimize interlayer delamination and applied in powder form to create a continuous single layer of multiple components. This structure offers HPCC an improved resistance to moisture ingression, chemical penetration, cathodic disbondment and impact. The strength of its adhesion to the substrate is ranked number one by both ASTM and CSA standards [20]. During construction, the coating's superior field-handling and flexibility characteristics allow for easier installation in cold weather. The properties of HPCC are superior to most other PE-based coatings. However, it is the most expensive coating of its kind.

## **2.3 Coating failures and cathodic protection shielding**

### ***2.3.1 Coating failure mechanisms***

In industry, coating integrity substantially impacts pipeline performance, longevity, and effectiveness. When the coating fails prematurely, the pipeline is attacked by corrosion, eventually resulting in catastrophic failures, huge repair costs, and a long down time. All this means a significant economic loss. Frequently, the coating failure is attributed to the materials

making a coating. In fact, the coating can also disintegrate throughout manufacturing, application, transportation, construction, and servicing [30]. During manufacturing, improper or incomplete cleaning and removal of rust or other surface contamination will lead to deficient coating adhesion to pipe surface. Dents, abrasions, and gouges due to improper handling during transportation can cause the coating to be defective. In the field, impact caused by excavation equipment and backfill materials can damage the coating and even the pipe in construction process. In addition, the presence of dirt, dust, chemicals, moisture and bacterial or even exposure to high-UV light in pipe service environment can pose threats to coating's integrity. In summary, coating failures can be resulted from improper formulation, poor surface preparation, inappropriate application, abnormal operating conditions, inadequate construction, incorrect specifications and coating defects. Statistics suggest that as much as 95% of all coating failures occur in surface preparation and application process [37].

In the case of buried pipelines under CP, the coating failure is always linked with the compatibility of the coatings with CP. The real problem is that the coating failure permits groundwater to come in direct contact with the steel surface, but block the CP current for corrosion protection. This phenomenon is called "CP shielding" (**Fig. 2.4**). As a result, corrosion can occur on the steel. Typical scenarios encountered during pipeline service are described below.

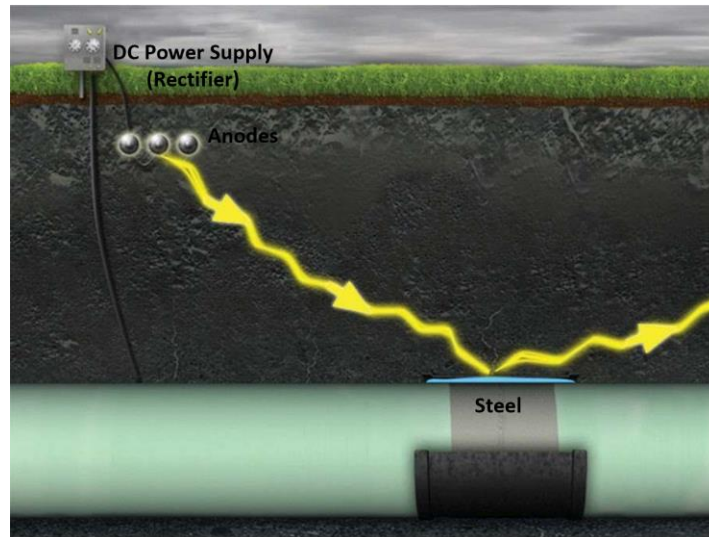


**Figure 2.4 Cathodic shielding problem in buried pipelines.**

### ***2.3.2 CP shielding by defect-free, disbonded coating membranes***

This scenario refers to CP shielding occurs when a defect-free coating disbonds due to lost adhesion to the pipe surface during service. This CP shielding is mainly attributed to the coating property. Highly dielectric coatings, such as PE and coal tar coating, can prevent the CP current from reaching the surface of the steel substrate, thereby failing to mitigate corrosion when electrolytes penetrate the steel/coating interface.

In the absence of holiday and discontinuity, the corrosion rate under coating disbondment would be low, as long as the coating's resistance remains high and its permeability for corrosive species keeps low [38]. Research has investigated the shielding effect of defect-free coating membranes on CP current. Kuang and Cheng [9] studied the CP shielding behavior of HDPE coating, and found that the CP current is shielded by intact HDPE. Water molecules are not absorbed into the coating. Fu and Cheng [19] measured the permeability of the HPCC to CP, and concluded that HPCC is impermeable to CP and shows a pure capacitive behavior.

### ***2.3.3 CP shielding at coating defects***

Microscopic defects in the form of pinholes could be introduced into coatings during manufacturing process. Mechanical damages are almost unavoidable during pipeline construction. Therefore, another scenario of CP shielding encountered in reality is that the CP current can be shielded from the pipelines where a small coating defect, such as pinhole or holiday, is generated [39]. The defects serve as channels for diffusion of water, moisture, and chemical species to reach the steel surface. Therefore, corrosion could occur locally.

It was demonstrated that pipeline corrosion at coating defects is dependent on the amount of CP current available and the size of the coating defect [40]. Therefore, when the applied CP potential is constant, the geometrical factor of coating defects plays an essential role in CP shielding. If the coating defects, especially their aspect ratio, are sufficiently large, the CP current is allowed to reach the defect base for corrosion protection. However, for narrow defects on thick coatings, the applied CP can be shielded, at least partially, from reaching the defect bottom. Perdomo and Song [40] investigated the impact of holiday size on CP under disbonded coating, and summarized that the amount of current required to establish a given cathodic potential is related to the holiday size.

For coating membrane that has a large defect, but the coating is tightly bound to the pipe, corrosion normally is not an issue. As the defect provides a pathway for corrosive species to reach the metal substrate, the CP system should be capable of providing continuous current to polarize the steel surface to a potential that stops corrosion of the steel. However, the coating disbondment frequently starts at coating defects. The CP current passing through the coating defects will elevate the pH of electrolyte at the holiday by cathodic reduction of water. The alkalization of local environment can weaken the coating adhesion to pipe substrate, resulting in

a rapid disbondment and coating breakdown. Thus, the pipeline will experience corrosion if the CP current is not adequate under coating disbondment. This coating disbondment caused by cathodic reaction is widely known as “cathodic disbondment”, which is an important mechanism for loss of coating adhesion [41].

#### ***2.3.4 CP shielding under disbonded coatings***

As mentioned above, the CP can facilitate coating disbondment at coating defects. When a coating is disbonded at small defects, the CP current can be shielded, either fully or partially, to reach the disbonding crevice, especially at the crevice bottom [42]. As a result, corrosion will occur on the steel if electrolyte generates under the disbonded coating. A large percentage of external corrosion, pitting corrosion and MIC is associated with this situation [9]. The CP shielding under disbonded coating has been the major issue with coated and cathodically protected pipelines [8].

Since CP current can be shielded partially or completely from reaching the disbondment, the steel under a disbonded coating, especially the disbondment bottom, can experience corrosion; while at the open holiday, the CP current may remain effective for corrosion protection. The separated anodic and cathodic reactions, which occur at the disbonded bottom and the open defect, respectively, will facilitate the occurrence of localized corrosion. This is the key mechanism that localized corrosion has frequently been observed under disbonded coating on a cathodically protected pipeline.

Generally, the CP performance under coating disbondment depends on the defect size and disbondment geometry. These two factors influence the flow of CP current towards the disbonded area, thus, the local corrosion protection of steels. Chen et al. [43] found that, with the

increasing distance from the open holiday, a higher cathodic polarization is required to achieve an appropriate CP level at the disbondment bottom. They also confirmed that a potential difference always exists between the open holiday area and inside disbondment, reducing the CP effectiveness. The CP permeation into the coating disbondment also depends on the AC stray current. Kuang and Cheng [44] found that a small AC current density, such as  $100 \text{ A/m}^2$ , can enhance the permeation of CP current into the coating disbondment, but with the increase in AC current density, the CP permeability decreases and the CP is blocked completely to reach the disbonding crevice when the AC current is up to  $500 \text{ A/m}^2$ .

## **2.4 Pipeline corrosion under coating disbondment**

### ***2.4.1 In the absence of microorganisms***

Disbondment is one of the most common coating failure modes on buried pipelines. It occurs when there is a loss of adhesion or detachment between the coating and the pipeline substrate. The environment developed under disbonded coatings is significantly different from the bulk soil, with higher cation concentrations and pH (in most cases), extremely low oxygen concentrations and a gradient of potentials and current density due to CP shielding [45]. In addition, the electrolyte trapped under disbonded coating is usually a thin layer of solution or even water condensate with a thickness in the range of tens of microns. The corrosion risk of the underlying pipeline can be localized corrosion, MIC or SCC, depending on the service environment, disbondment geometry, and the compatibility of coatings with CP [46].

Research has been conducted to study external corrosion of buried pipelines under disbonded coatings with or without a holiday. The permeation of molecular (e.g., water vapor,  $\text{O}_2$  and  $\text{CO}_2$ ) and ionic (e.g.,  $\text{Cl}^-$ ,  $\text{HCO}_3^-$ ) species to the pipe surface has been attributed to be one of the

leading causes that initiate corrosion under disbonded coating. Without a holiday in the disbonded coating, the underlying pipeline corrosion rate was found to be extremely small, within a few micrometers per year [38]. While, with a holiday contained in the disbonded coating, the corrosion rate of underneath pipeline can be significant. As stated above, the CP shielding may cause the separation of anodic and cathodic reactions, which occur at the disbonded bottom and the open defect, respectively. Localized corrosion cells will then form, and rusting and pitting can proceed. Moreover, the areas on the pipeline where the coating has defects are most likely sensitive to DC and AC interference corrosion.

Based on the compatibility of the coatings to CP, pipeline coatings can be divided into two systems: shielding and non-shielding coatings. When disbondment occurs, most types of coating shield CP current from reaching the steel. Field observations have indicated that corrosion occurs on pipelines under disbonded shielding coatings, especially at the bottom of the disbondment. The electrolyte generated by permeation of water, chemicals, CO<sub>2</sub>, etc. from seams (for wrapped tape coating) or local openings (usually at pipeline welds) into the disbondment. The trapped electrolyte under disbonded shielding coating, such as PE tape, is usually a diluted, near-neutral pH bicarbonate solution with a low oxygen content. Both field experiences and lab tests demonstrate that this environment could result in a near-neutral pH SCC on pipelines, where both anodic dissolution reaction and the hydrogen effect are involved in the crack propagation.

While certain types of pipeline coatings allow CP current to penetrate if disbondment occurs and water penetrates between the coating and pipe surface. They are called “non-shielding” pipeline coatings. FBE has been accepted as a CP compatible coating (non-shielding). Non-shielding coatings are permeable to CP current, which protect the pipe steel from corrosion when corrosive electrolyte is generated under the disbondment. However, because of hydroxyl ions

generated by the CP-driven cathodic reduction of water, the pH of the trapped electrolyte is elevated under disbonded coating. The local alkaline environment will damage the coating adhesion to steel substrate, further enlarging the disbonded area (i.e., cathodic disbondment). Moreover, the high pH environment under non-shielding coating (such as asphalt) can cause high pH SCC of pipeline if corrosive species and oxygen could penetrate through the coating to reach the pipeline steel surface, forming a concentrated carbonate/bicarbonate/chloride environment. Therefore, although coating disbondment is a more critical issue for impermeable coatings that shield CP from reaching the steel surface for corrosion protection, the cathodic disbonding of permeable coatings is also a serious threat to pipeline integrity.

Actually, the CP can become somewhat shielded regardless of whether the coating is shielding or non-shielding. Corrosion products, such as  $\text{Fe}(\text{OH})_2$ , are generated in the alkaline environment that is formed due to CP-driven electrochemical cathodic reactions. The corrosion products deposit in the disbondment because of the limited diffusion in the crevice space will block the penetration of CP current into the bottom of the disbondment. Therefore, even for the permeable coating such as FBE, the CP shielding under coating disbondment can still occur.

#### ***2.4.2 In the presence of microorganisms***

Microorganisms exist extensively in soil environments due to their ability to grow and reproduce at a rapid rate. The corrosion that is influenced by the presence and activities of microorganisms is widely known as MIC. MIC under disbonded coating has been identified as one of the major corrosion types occurring on underground pipelines, leading to serious consequences such as perforation, leaking and environmental damage [47]. Predominantly four microbial species are associated with pipeline MIC: SRB, acid-producing bacteria (APB), iron-

reducing bacteria (IRB), and iron-oxidizing bacteria (IOB). Among them, SRB have been recognized as the most predominant microbes attributing to MIC for pipelines.

SRB are anaerobes and key players in anaerobic pipeline corrosion. They gain energy for growth by reduction of sulfate to hydrogen sulphide ( $H_2S$ ) with electrons usually derived from the degradation of organic matters. It was reported that SRB are able to accelerate the corrosion reaction kinetics [24]. The contributions of SRB to pipeline MIC are frequently explained by two mechanisms described below. The schematic illustration of SRB-induced pipeline MIC mechanisms is shown in **Fig. 2.5**.

**Electrical microbiologically influenced corrosion (EMIC):** SRB attack pipes by withdrawal of electrons directly from iron. The anodic dissolution of iron results from electron consumption by sulfate reduction. EMIC allows SRB to utilize iron more efficiently as an electron donor by direct uptake of electrons from the iron oxidation.

**Chemical microbiologically influenced corrosion (CMIC):** SRB damage steels indirectly through excreting the corrosive chemicals,  $H_2S$ , formed by the sulfate reduction with organic compounds or hydrogen.

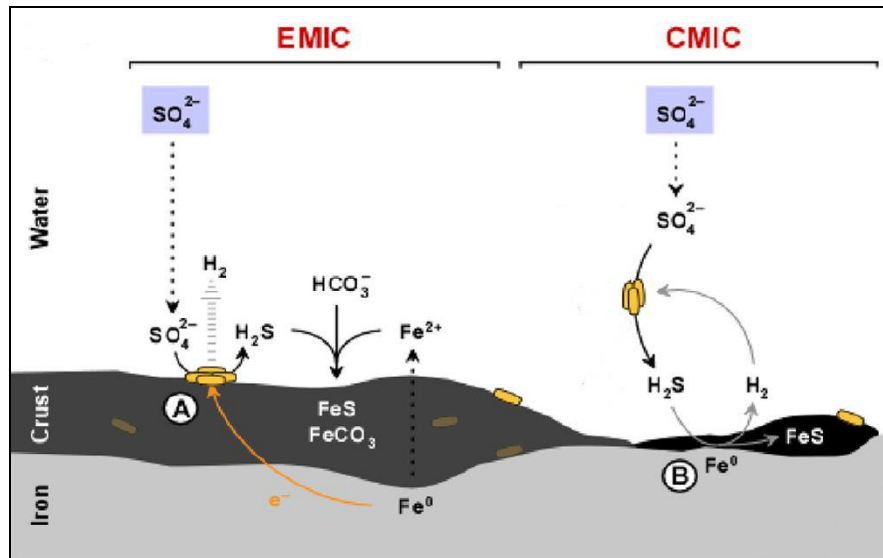


**Figure 2.5 Schematic illustration of EMIC and CMIC [24].**

In SRB-induced corrosion, iron sulfides (FeS) are the primary corrosion products and they play a dual role in pipeline corrosion. The formation of FeS may reduce corrosion in some cases, while accelerate corrosion in others. Newman et al. [48] stated that the formation of protective FeS films occurs when dissolved sulfide concentrations exceed the concentration of dissolved ferrous ions at the unreacted metal surface, i.e., usually at high concentrations of dissolved sulfide. The rupture of FeS films and local re-exposure of steels results in repaid pitting corrosion unless additional sulfide seals the exposed site [49].

Under coating disbondment, the trapped electrolyte usually has a low oxygen content, which is favorable for SRB growth. CP cannot effectively protect the pipe steel from SRB attack due to the shielding effect by the disbonded coating. Moreover, the coating components, such as asphalt, heat shrink sleeves and dual layer PE, can provide primary nutrients for SRB multiplication. Thus, the SRB-induced corrosion can occur under the coating disbondment. Field

investigations demonstrated that a higher number of SRB was counted at the corrosion sites under the disbonded coating than that in the bulk soil. It was also shown that a high degree of SRB corrosion occurs under most disbonded coatings. For example, Li et al. [22] conducted detailed field surveys and laboratory analysis of corroded pipes buried in anaerobic soils, and identified the presence of high numbers of SRB under the disbonded coatings at weld joints.

There have been some work investigating the SRB-induced corrosion of pipelines under disbonded coating. Li et al. [22] found that the SRB-induced corrosion under coating disbondment is a localized, pitting-type corrosion in most cases. Xu et al. [50] investigated the effect of SRB on crevice corrosion under disbonded coating in soil-extracted solutions, and found that, which causes an alkalization of the solution in the crevice. Zhao et al. [23] proposed that the biogenic sulfide led to formation of local galvanic cells and contributed to cathodic depolarization. Chen et al. [51] found that, in the presence of SRB in the trapped solution under coating, the biofilm formation and sulfide deposition caused an increase in the potential difference between the inside and outside of the disbondment, compared to the sterilized solution. Liu and Cheng [52] concluded that the CP facilitated the bacterial attachment to the steel, and a layer of biofilm formed on the steel decreased the CP effectiveness for corrosion protection.

In summary, while some works have been conducted to understand SRB induced MIC of pipeline under disbonded coatings, the tests were mostly performed in bulk solutions. There has been limited work to study the MIC in thin layers of solution, which is more representative of the reality for disbonded coatings.

## **Chapter Three: Compatibility of Polyethylene Coating with Cathodic Protection and the Corrosion of Cathodically Protected Pipelines under Disbonded Coating**

### **3.1 Introduction**

Ideally, coatings provide the first line of barrier to protect pipelines from corrosion attack. CP serves as a back up to prevent corrosion occurring either at coating defects, such as pinholes and holidays, or under disbonded coating [7, 10, 43, 53, 54]. However, in reality, the CP current can become fully or partially shielded from reaching the disbonded area when the coating disbonds at small defects or at a defect-free area [9, 19, 43, 55, 56]. As a result, pipeline corrosion occurs when electrolytes penetrate the coating disbondment [38, 55, 57, 58].

There have been works to investigate the compatibility of PE coating with CP and the corrosion behavior of cathodically protected pipelines under coating disbondment. For example, Kuang and Cheng [9] studied the CP shielding behavior of PE coating, and found that PE was a CP-shielding coating. Eslami et al. [59] summarized that the corrosion rate of pipeline steel under PE coating disbondment could be significantly different to that in bulk environments, and the corrosion rate was a function of carbon dioxide (CO<sub>2</sub>) and the level of CP at the holiday of the coating disbondment. To date, there has been few works to systematically characterize the permeability of PE coatings to CP and the corrosion of pipelines at various modes of coating failures. There have also been limited reports regarding the effects of coating thickness, holiday size and disbondment geometry on CP permeability under disbonded PE coatings.

In this work, the permeability of a PE coating to CP at various modes of coating failure was determined, and the corrosion mechanism of an X52 pipeline steel under disbonded PE coating

was investigated in a simulated soil solution. The CP current was measured by potentiostatic polarization and a microammeter. A voltmeter with a high input impedance was used to measure the potential. The pH of the electrolyte trapped under the disbonded PE coating was monitored by a pH meter. The corrosion morphology was characterized by optical microscopy. The parametric effects on CP permeability of the PE coating and pipeline corrosion under coating disbondment were determined.

## **3.2 Experimental**

### ***3.2.1 Coating, steel and solution***

HDPE membranes used in this work were supplied by Enbridge Pipelines. Steel specimens were cut from an X52 pipe, with a chemical composition (wt. %): 0.24 C, 1.4 Mn, 0.45 Si, 0.025 P, 0.015 S, 0.10 V, 0.05 Nb, 0.04 Ti and Fe balance. The specimens were welded to a copper wire and sealed with epoxy, leaving a working area of 1 cm × 1 cm. The sealing was controlled carefully to ensure that there was no bubble and groove generating at the epoxy/steel interface. The exposed face of the specimen was sequentially ground with #240, #400, #600, #800, and #1000 grit emery papers, cleaned by anhydrous alcohol and acetone, and dried in air.

A simulated soil solution with the identical composition to the extracted solution from a clay soil in Regina, Canada was used in this work. To analyze the extracted soil solution, the international standard ISO 11048 [60] was followed. The soil sample was dried in an oven at 60 °C for 24 h and was then mixed with deionized water in a container under stirring at room temperature for 24 h. The mass ratio of the soil to the deionized water was 1:5. The mixture was added into centrifuge tubes which were installed in a centrifuge under a rotating speed of 4000 r/min for 10 min. After that, the upper layer of the solution in the tubes was analyzed by ion

chromatography. The composition of the extracted soil solution is shown in **Table 3.1**. The simulated soil solution was prepared by analytic grade chemicals and deionized water, including (g/L) 0.0755 NaHCO<sub>3</sub>, 0.0092 NaCl, 0.0014 NaNO<sub>3</sub>, 0.0773 Na<sub>2</sub>SO<sub>4</sub>, 0.0619 K<sub>2</sub>SO<sub>4</sub>, 1.116 CaSO<sub>4</sub>·2H<sub>2</sub>O, 0.662 MgSO<sub>4</sub>·7H<sub>2</sub>O. The solution was purged with 5% CO<sub>2</sub>/N<sub>2</sub> gas to maintain the pH value of 6.0 to 6.5. All tests were conducted at ambient temperature (~22°C).

**Table 3.1 Chemical composition of the extracted solution from Regina clay soil.**

Ions	Na <sup>+</sup>	Ca <sup>2+</sup>	Mg <sup>2+</sup>	K <sup>+</sup>	SO <sub>4</sub> <sup>2-</sup>	NO <sub>3</sub> <sup>-</sup>	Cl <sup>-</sup>	HCO <sub>3</sub> <sup>-</sup>
Concentration (mg/L)	49.70	259.80	65.21	27.82	965.85	1.01	5.41	55.19

### ***3.2.2 Measurements of CP permeability of the PE coating***

Two self-designed test rigs enabling measurements of the CP permeability of PE coating membranes without and with a holiday are shown in **Fig. 3.1**. In **Fig. 3.1a**, two testing chambers were separated by a defect-free PE coating membrane with varied thicknesses, and in **Fig. 3.1b**, a PE coating membrane with 2.0 mm in thickness contained a holiday with varied sizes. Three coating thicknesses, i.e., 1.0 mm, 1.5 mm and 2.0 mm, were selected to determine the effect of coating thickness on CP permeability of the defect-free PE coating in **Fig. 3.1a**. Five holiday diameters, i.e., 10.0 mm, 4.0 mm, 2.0 mm, 1.0 mm and 0.5 mm, were selected to investigate the effect of holiday size on CP permeability of the coating containing a holiday in **Fig. 1b**. In the two test rigs, a gap of 5 mm between the coating membrane and the steel electrode simulated the disbonding crevice under the coating.

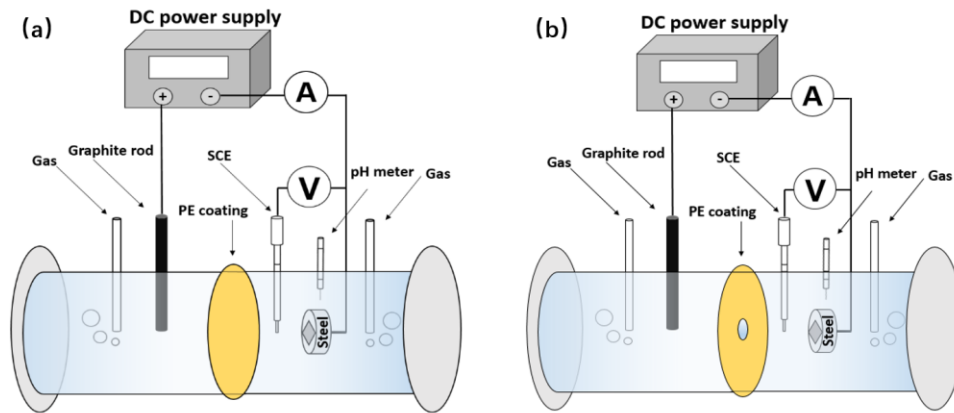


**Figure 3.1** Schematic diagram of the self-made test rigs to measure the CP permeability of (a) disbonded defect-free PE coating (with varied thicknesses), and (b) a disbonded PE coating (2.0 mm in thickness) with a holiday with varied sizes.

**Fig. 3.2** shows the experimental setup to measure the CP permeability at varied disbonding depths from the open holiday under disbonded PE coating in the simulated soil solution. The dimension of the Perspex sheet was 250 mm × 50 mm × 5.8 mm. To prepare an artificial disbondment, the PE coating (2.0 mm in thickness) was applied on adhesion zones of the Perspex sheet using a double-sided self-adhesive tape. The gap between the coating and the steel was determined by the thickness of the tape, which was verified with a coating thickness gauge. The thickness of the created gap was defined as the disbonding thickness. Both ends of the Perspex/coating assembly were sealed with epoxy. A hole (10.0 mm in diameter) was opened on the coating to simulate an open holiday. Six potential/pH micro-probes were installed at the distances of 30 mm, 60 mm, 90 mm, 120 mm, 150mm and 180 mm from the defect. The distance of the probing position to the open holiday was defined as the disbonding depth. To further investigate the effect of disbonding thickness on CP permeability at varied disbonding depths

from the open holiday under disbonded coating, the tape with three known thicknesses, i.e., 120  $\mu\text{m}$ , 240  $\mu\text{m}$  and 360  $\mu\text{m}$ , was layered to establish the desired disbonding thicknesses.

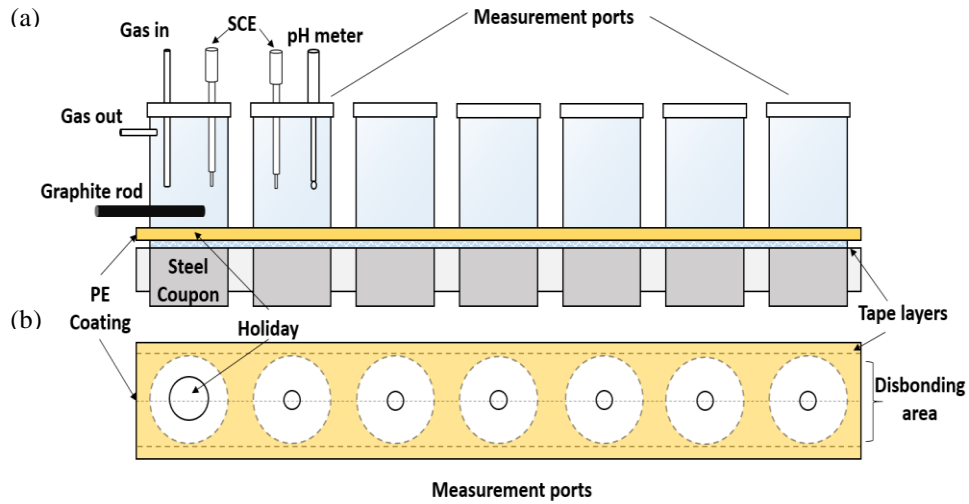


**Figure 3.2 Schematic diagrams of the experimental setup to measure the CP permeability under disbonded PE coating in the simulated soil solution (a - front view, b – top view without measurement ports).**

In the three test units, a carbon rod was used as auxiliary anode, the steel electrode as cathode, and the copper sulfate electrode (CSE) as reference electrode (RE). The RE was immersed into the Luggin capillary, with a 3-mm distance to the steel electrode. A CP potential of -925 mV (CSE) was applied on the steel electrode through an external direct current (DC) power supply. The CP current was measured by a Solartron 1280C electrochemical workstation in **Fig. 3.1a**, where the steel specimen was used as working electrode (WE), a carbon rod as counter electrode (CE) and a CSE as RE. In **Fig. 3.1b** and **Fig. 3.2**, the CP current was measured by a microammeter. A voltmeter with a high input impedance was used to measure the potential. The

pH value of the solution was monitored through a pH meter. During testing, a continuous 5% CO<sub>2</sub>/N<sub>2</sub> gas flow was maintained in the solutions in three cells.

### ***3.2.3 Surface characterization***

After testing, the steel electrodes under the coating were removed and rinsed with deionized water and dried with pure N<sub>2</sub> gas flow. The surface morphology of the steel electrodes after the test was characterized by an optical microscope.

## **3.3 Results**

### ***3.3.1 CP permeability of defect-free PE coating membranes with various thicknesses***

**Fig. 3.3** shows the optical views of the steel specimens after 30 days of testing in the simulated soil solution using the setup in **Fig. 3.1a**, where the PE coating membranes with various thicknesses are used and a CP potential of -925 mV (CSE) is applied. It is seen that without the coating the applied CP can fully protect the steel from corrosion, while the steel under the disbanded PE coating corrodes after 30 days of testing in the soil solution even the CP is applied. Obviously, the applied CP does not provide protection to the steel under the PE coating. Moreover, the coating thickness does not affect the steel corrosion visually.

**Fig. 3.4** shows the CP current density measured on X52 steel electrode in the simulated soil solution separated by a PE coating membrane with varied thicknesses under the CP potential of -925 mV (CSE). It is seen, at individual coating thicknesses, the current density tends to increase negatively with time, indicating the increased CP current permeation through the coating. At individual testing times, the cathodic current through the coating decreases slightly with the increasing coating thickness and the current density difference between each thickness becomes

smaller with the coating thickness increases. For example, after 30 days of testing, the cathodic currents measured are about  $-0.020$ ,  $-0.017$  and  $-0.016$   $\text{nA}/\text{cm}^2$  when the coating thicknesses are 1.00 mm, 1.50 mm and 2.00 mm, respectively. Thus, the CP current permeation is reduced as the coating thickness increases. It is further noticed that all the measured current densities are cathodic, indicating that the PE coating does not behave like an ideal capacitor [9]. Although the CP current can permeate through the coating, the recorded cathodic current is negligible (i.e., less than  $0.3$   $\text{nA}/\text{cm}^2$ ), compared to the average polarization current density of  $-16.25$   $\mu\text{A}/\text{cm}^2$  of a bare X52 steel under the applied CP potential of  $-925$  mV (CSE) in the same soil solution, as shown in **Fig. 3.5**.

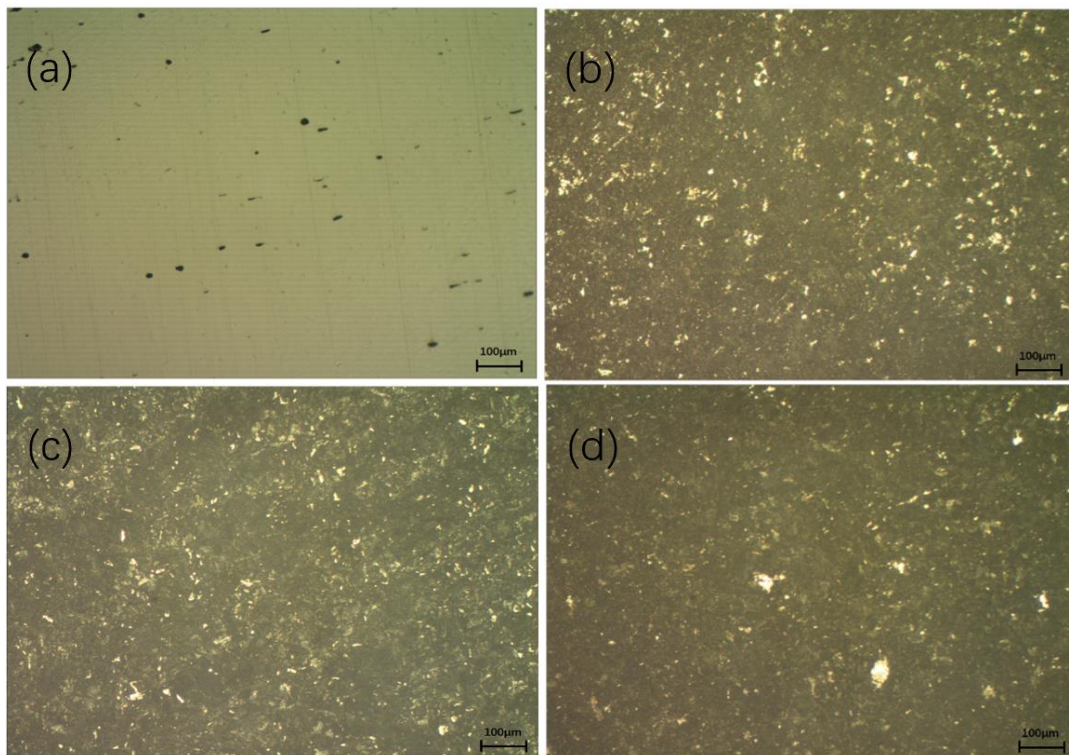


**Figure 3.3** Optical views of the steel specimens after 30 days of testing in the simulated soil solution which is separated by a PE coating membrane with varied thicknesses (a – 0.0 mm b – 1.0 mm, c – 1.5 mm, d – 2.0 mm) in Fig. 3.1a, while a CP potential of  $-925$  mV (CSE) is applied.

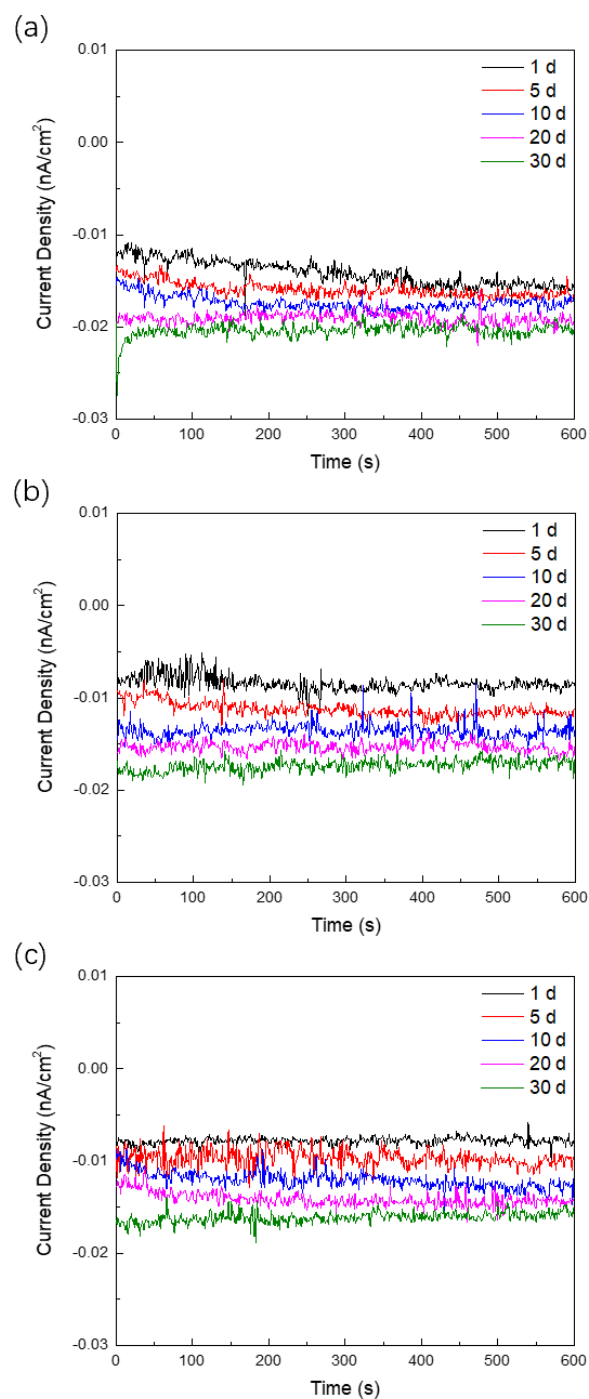


**Figure 3.4 CP current densities measured on X52 steel electrode in the simulated soil solution separated by a PE coating membrane with varied thicknesses of (a) 1.0 mm, (b) 1.5 mm and (c) 2.0 mm under the CP potential of -925 mV (CSE).**

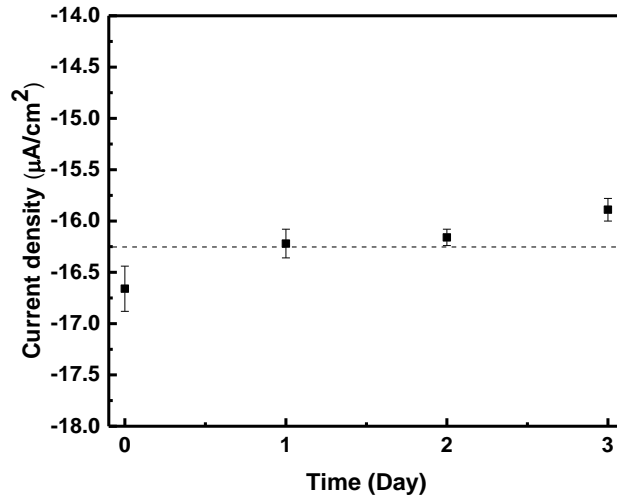


**Figure 3.5 Polarization current density of X52 steel at the applied CP potential of -925 mV (CSE) in the simulated soil solution.**

To further characterize the CP shielding by the disbonded PE coating, the potential of the steel in the simulated soil solution separated by the PE coating with various thicknesses as a function of time is measured using the setup in **Fig. 3.1a**, and the results are shown in **Fig. 3.6**. It is seen that the potential of the steel is much less negative than the applied CP potential of -925 mV (CSE), indicating that the steel is shielded from the CP current by the PE coating membrane. With the increasing time, the potentials increase slightly and reach steady values of about -790 mV (CSE), which is approximately the corrosion potential of X52 pipeline steel in the simulated soil solution [61]. Thus, the CP current, even it is applied, would be shielded from reaching the steel by the PE coating for corrosion protection.

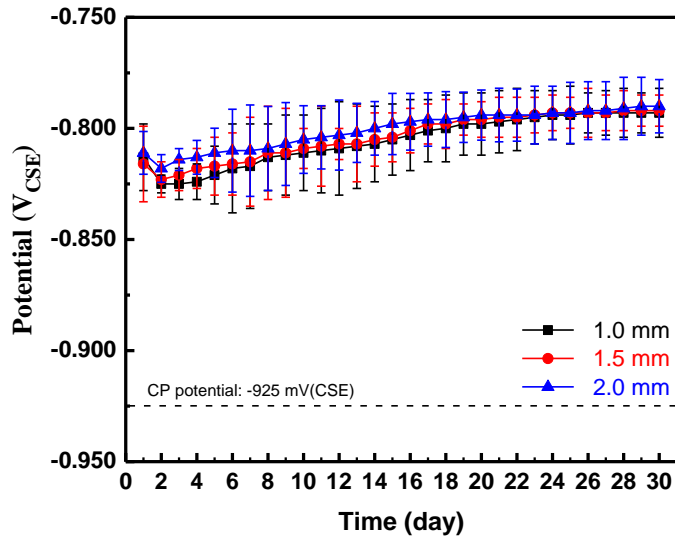


**Figure 3.6 Potential of the steel in the simulated soil solution separated by the PE coating membrane with varied thicknesses as a function time.**

**Fig. 3.7** shows the pH of the soil solution which is separated by the PE coating membrane with varied thicknesses as a function of time at the applied CP potential of -925 mV (CSE). It is seen that all solution pH remains at about 6.4 during 30 days of testing. Generally, the pH value of the soil solution would be elevated due to the CP enhanced water reduction if the CP current permeates through the coating [42]. In this work, there is no obvious increase of the solution pH, indicating that the CP current is blocked by the PE coating from reaching the soil solution side.

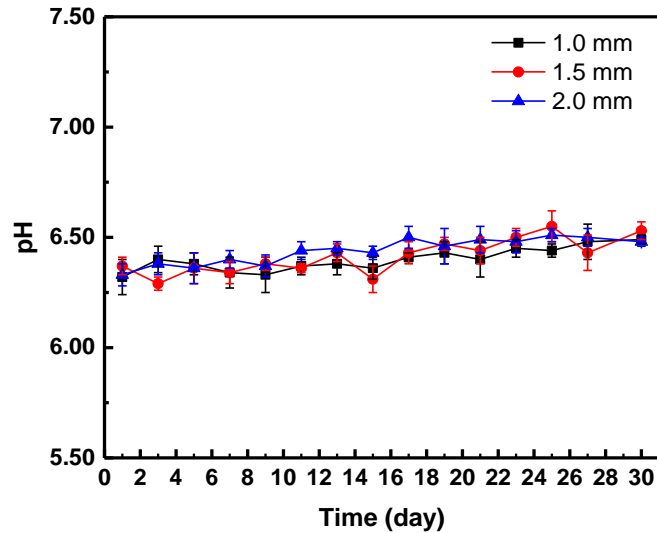


**Figure 3.7** pH of the soil solution which is separated by the PE coating membrane with varied thicknesses as a function of time at the applied CP potential of -925 mV (CSE).

### 3.3.2 CP permeability of PE coating containing a holiday with varied sizes

**Fig. 3.8** shows the optical views of the steel specimen after 15 days of testing in the simulated soil solution separated by a PE coating membrane containing a holiday with varied sizes (i.e., setup in **Fig. 3.1b**), where a CP potential of -925 mV (CSE) is applied at the holiday. It is seen that there is no obvious corrosion observed on the steel specimens when the coating holiday is sized 10 mm and 4 mm in diameter. This indicates that CP current can penetrate through the holiday and protect the steel from corrosion. However, when the holiday is 2 mm in diameter, the steel is corroded slightly, and as the holiday is as small as 1 mm and 0.5 mm in diameter, the steel suffers from corrosion apparently. Thus, the applied CP is partially or fully shielded from reaching the steel for corrosion protection. The results show that the CP permeation through a

coating holiday depends on its size. In this work, when the holiday is as small as 2 mm in diameter, the CP current starts to be shielded.

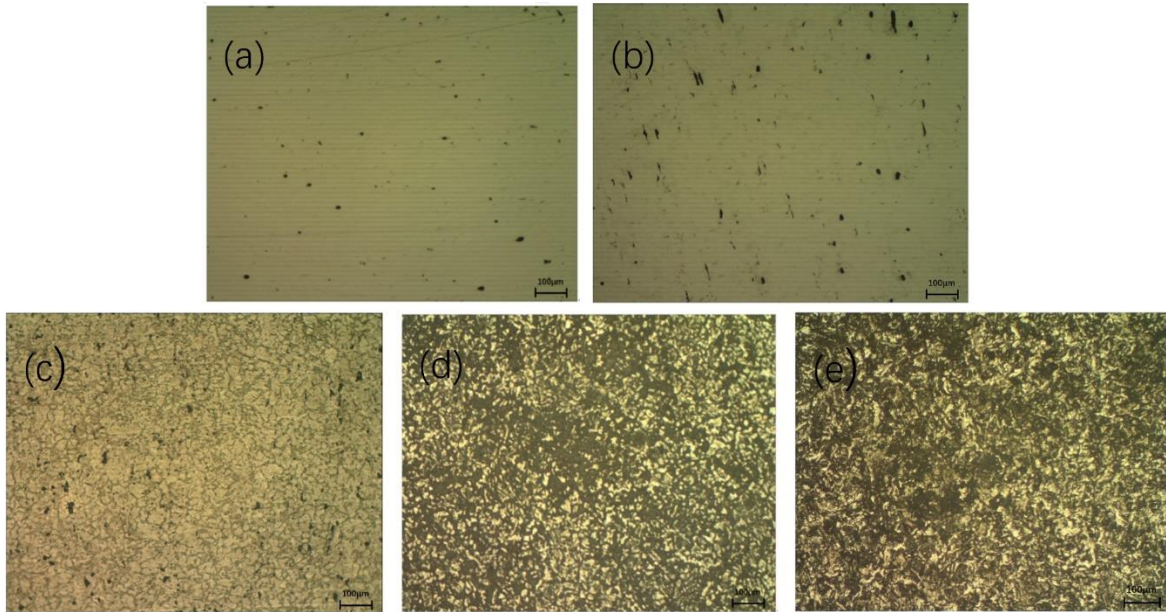


**Figure 3.8** Optical views of the steel specimens after 15 days of testing in the simulated soil solution separated by a PE coating membrane containing a holiday with varied sizes (a) 10 mm, (b) 4 mm, (c) 2 mm, (d) 1 mm, (e) 0.5 mm in Fig. 3.1b, while a CP potential of -925 mV (CSE) is applied at the holiday.

**Fig. 3.9** shows the cathodic current density measured on the steel in the simulated soil solution separated by the PE coating containing a holiday with varied sizes at the CP potential of -925 mV (CSE) as a function of time. It is seen that, initially, the cathodic current density of the steel is close to the required CP current density for a full CP (i.e.,  $-16.25 \mu\text{A}/\text{cm}^2$  as seen in **Fig. 3.5**) when the holiday diameter is 10 and 4 mm. This indicates that there is sufficient CP current

permeating through the holiday to protect the steel. The cathodic current density drops rapidly and remains at a relatively stable value of around  $-2.7 \mu\text{A}/\text{cm}^2$ , which is due to the formation of calcareous deposit on the steel surface [28]. Whereas the cathodic current density is much lower than the required CP current density for coating holidays with the diameter of 2 mm, 1mm and 0.5 mm, indicating the CP current is partially or fully blocked by the small holidays.

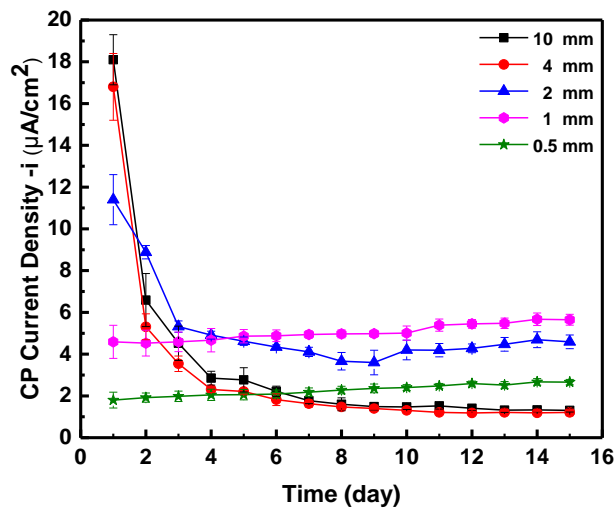


**Figure 3.9 CP current density measured on the steel in the simulated soil solution separated by the PE coating containing a holiday with varied sizes at the CP potential of -925 mV (CSE) as a function of time.**

**Fig. 3.10** shows the potential of the steel in the soil solution separated by a PE coating containing a holiday with varied sizes at the CP potential of -925 mV (CSE) as a function of time. It is seen that, with the increasing holiday size, the potential is more negative. The potential of the steel reaches the steady-state value of about -925 mV (CSE) (i.e., the applied CP potential) when the holiday diameter is 10 mm and 4 mm. Thus, the CP completely penetrates through the

holidays. For the holidays with the diameter of 2 mm, 1 mm and 0.5 mm, the potential of the steel is less negative and is steady at about -900, -850 and -820 mV (CSE), respectively. This demonstrates that the CP is shielded, at least partially, by the small holidays.

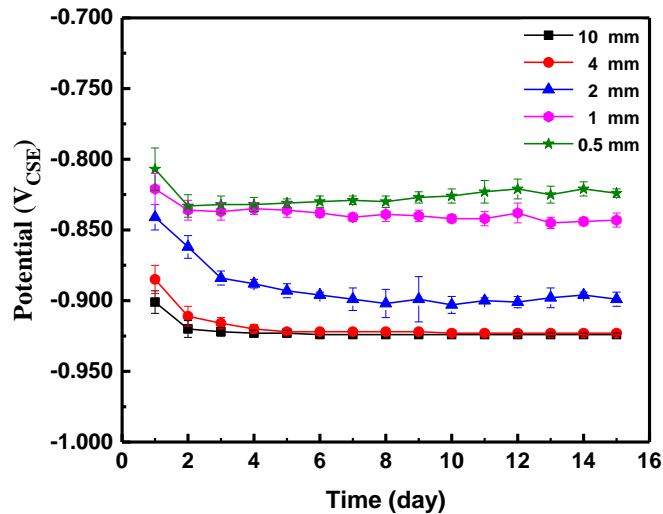


**Figure 3.10 Potential of the steel in the soil solution separated by a PE coating containing a holiday with varied sizes at the CP potential of -925 mV (CSE) as a function of time.**

**Fig. 3.11** shows the pH of the soil solution which is separated by the PE coating containing a holiday with varied sizes as a function of time at the applied CP potential of -925 mV (CSE). It is seen that, although the 5% CO<sub>2</sub>/N<sub>2</sub> purging decreases the solution pH, the pH of the soil solution increases with large holiday diameters such as 10 and 4 mm. This is due to the fact that the large holidays allow CP to penetrate, at least partially, as confirmed by the potential measurements, to enhance the water reduction to elevate the solution pH [28].

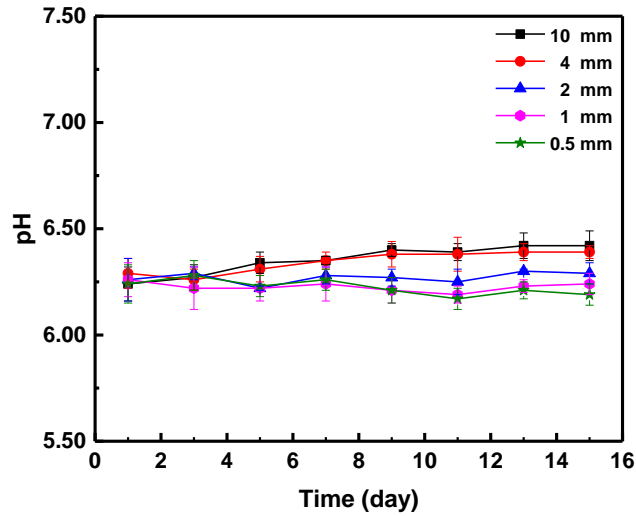


**Figure 3.11** pH of the soil solution which is separated by the PE coating containing a holiday with varied sizes as a function of time at the applied CP potential of  $-925$  mV (CSE).

### *3.3.3 CP permeability at varied disbonding depths from the open holiday under PE coating disbondment*

**Fig. 3.12, Fig. 3.13 and Fig. 3.14** show the optical images of the steel electrodes at different disbonding depths from the open defect (diameter in 10 mm) under disbonded PE coating with disbonding thickness of 120, 240 and 360  $\mu\text{m}$ , respectively, after testing for 15 days, where a CP potential of  $-925$  mV (CSE) is applied at the holiday. It can be noticed that there is no obvious corrosion on the steel electrode at the open defect after 15 days. This indicates the CP current can reach the steel at the open holiday and protect the steel from corrosion. However, the corrosion of the steel electrode tends to be more serious with the increasing disbonding depth under the coating disbondment, indicating the CP shielding becomes more apparent as the disbonding

depth increases. At individual disbonding depths, as the disbonding thickness increases, the corrosion products on the steel electrode surface reduce slightly. This demonstrates the shielding effect can be mitigated by the increasing disbonding thickness. In the morphology, the dark area is corroded seriously, and the white area is the lightly corrode area. There is no obvious pitting corrosion on the steel surface, indicating it is general corrosion when the steel electrode immersion in the soil solution.

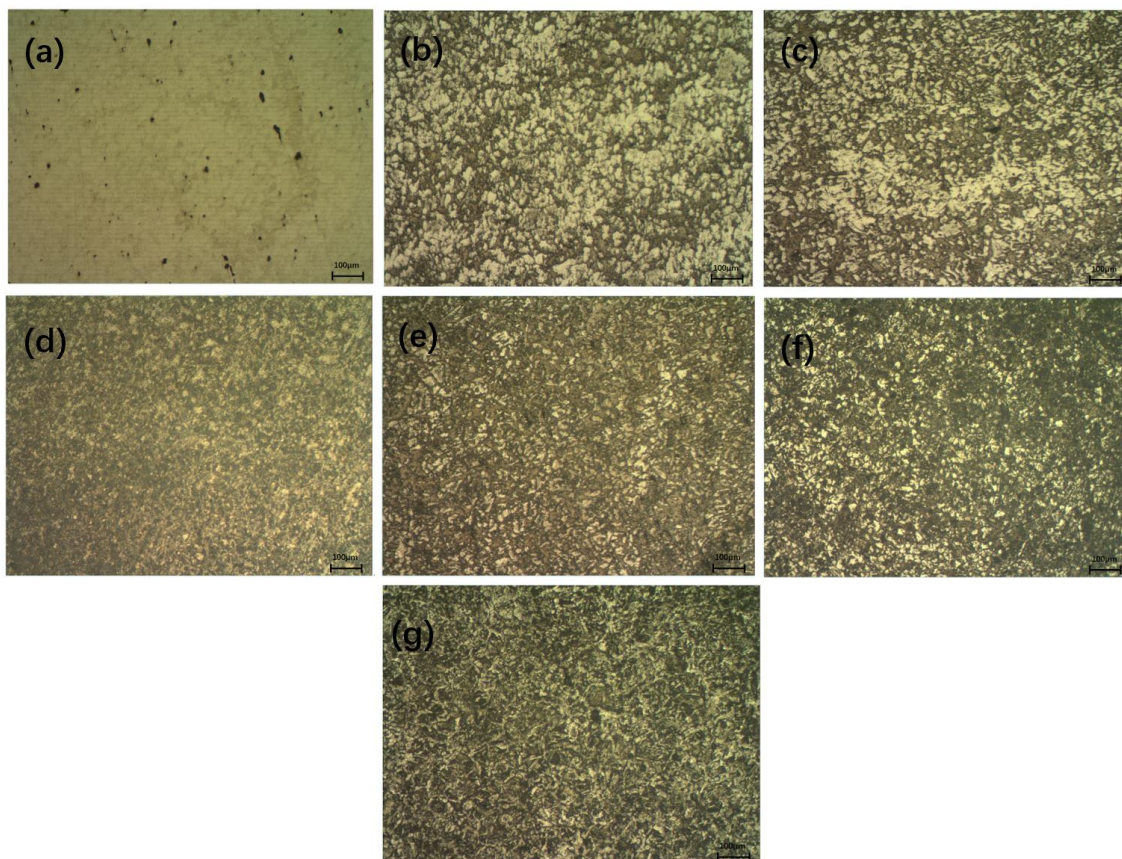


**Figure 3.12 The morphology of the steel surface at varied disbonding depths (a) 0 mm, (b) 30 mm, (c) 60 mm, (d) 90 mm, (e) 120 mm, (f) 150 mm and (g) 180mm from the open defect (defect of 10 mm) under disbonded PE coating (disbonding thickness of 120 μm) after testing for 15 days, where a CP potential of -925 mV (CSE) is applied at the holiday.**

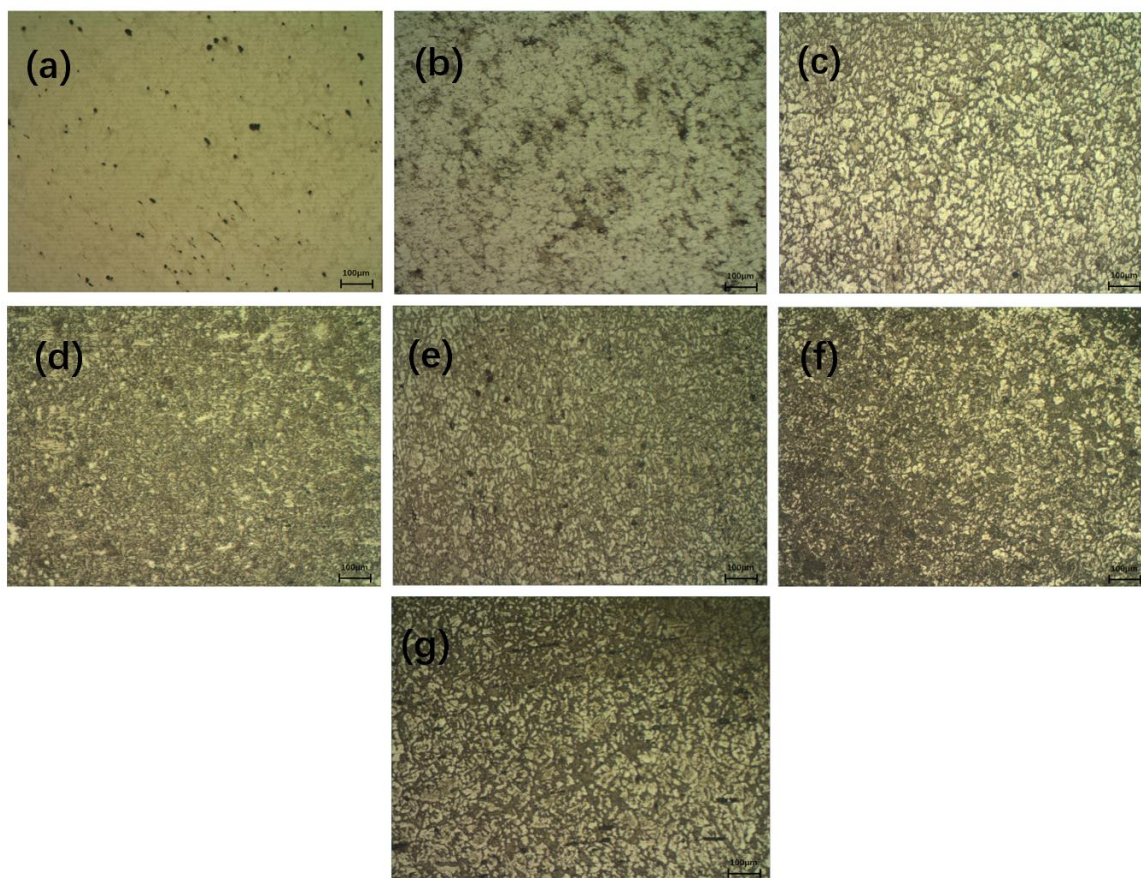


**Figure 3.13 The morphology of the steel surface at varied disbonding depths (a) 0 mm, (b) 30 mm, (c) 60 mm, (d) 90 mm, (e) 120 mm, (f) 150 mm and (g) 180mm from the open defect (defect of 10 mm) under disbonded PE coating (disbonding thickness of 240  $\mu\text{m}$ ) after testing for 15 days, where a CP potential of -925 mV (CSE) is applied at the holiday.**

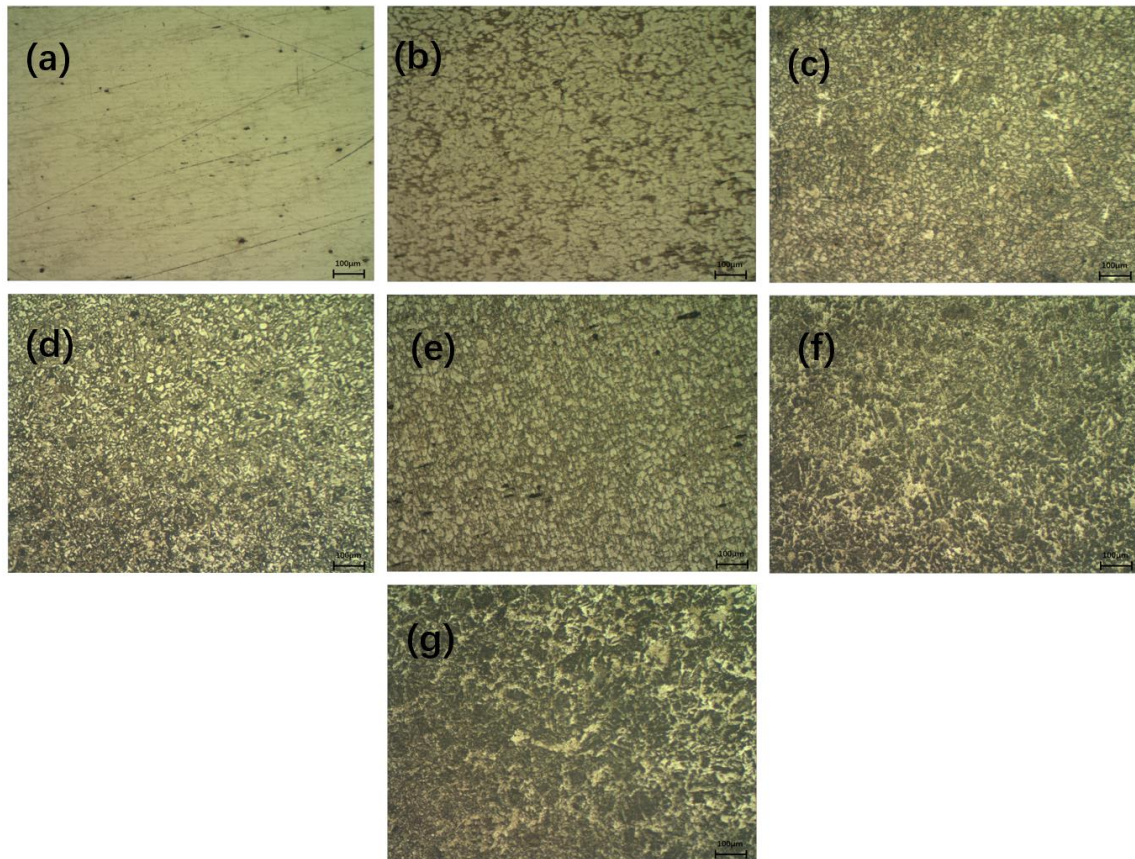


**Figure 3.14** The morphology of the steel surface at varied disbonding depths (a) 0 mm, (b) 30 mm, (c) 60 mm, (d) 90 mm, (e) 120 mm, (f) 150 mm and (g) 180mm from the open defect (defect of 10 mm) under disbonded PE coating (disbonding thickness of 360  $\mu\text{m}$ ) after testing for 15 days, where a CP potential of -925 mV (CSE) is applied at the holiday.

**Fig. 3.15** shows the time dependence of cathodic current density of X52 steel under disbonded PE coating at varied disbonding depths from the open holiday (10 mm in diameter) with various disbonding thicknesses in the simulated soil solution, where a CP potential of -925 mV (CSE) is applied at the holiday. It is seen that the cathodic current density is close to the required CP current density for a full CP (i.e.,  $-16.25 \mu\text{A}/\text{cm}^2$  as seen in **Fig. 3.5**) at the open holiday, while

the value of current density under the disbonded PE coating is much less than that. This demonstrates that the CP is applied on the holiday but is blocked by the coating disbondment. Moreover, at individual disbonding depth, the current density increases slightly with the increase in the disbonding thickness. This indicates that, although the coating disbondment still effectively shields the CP current from reaching the steel for corrosion protection, the increasing disbonding thickness favors the CP current permeation under coating disbondment.

**Fig. 3.16** shows the time dependence of the distribution of local potential under disbonded PE coating at varied disbonding depths from the open holiday (diameter in 10 mm) with various disbonding thicknesses in the simulated soil solution, where a CP potential of -925 mV (CSE) is applied at the holiday. It is seen that, generally, the potential decreases rapidly after testing in the first few days, and then reach a relatively steady value. At the open holiday, the potential is the applied CP potential, therefore the CP completely reach the steel electrode under the open defect. While under the coating disbondment, the potential tends to be less negative and with increase in the disbonding depth, the potential shifts toward the positive direction. Identical to previous results, the CP shielding tends to be more significant as the disbonding depth increases. Moreover, at individual disbonding depth, the potential tends to be more negative with the increasing disbonding thickness. For example, at the disbonding depth of 180 mm from the open holiday, the potentials are about -0.79 V, -0.82 V and -0.83 V (CSE) at the disbonding thicknesses of 120  $\mu\text{m}$ , 240  $\mu\text{m}$  and 360  $\mu\text{m}$ , respectively. Thus, the permeability of CP current increases with the disbonding thickness becomes wider.

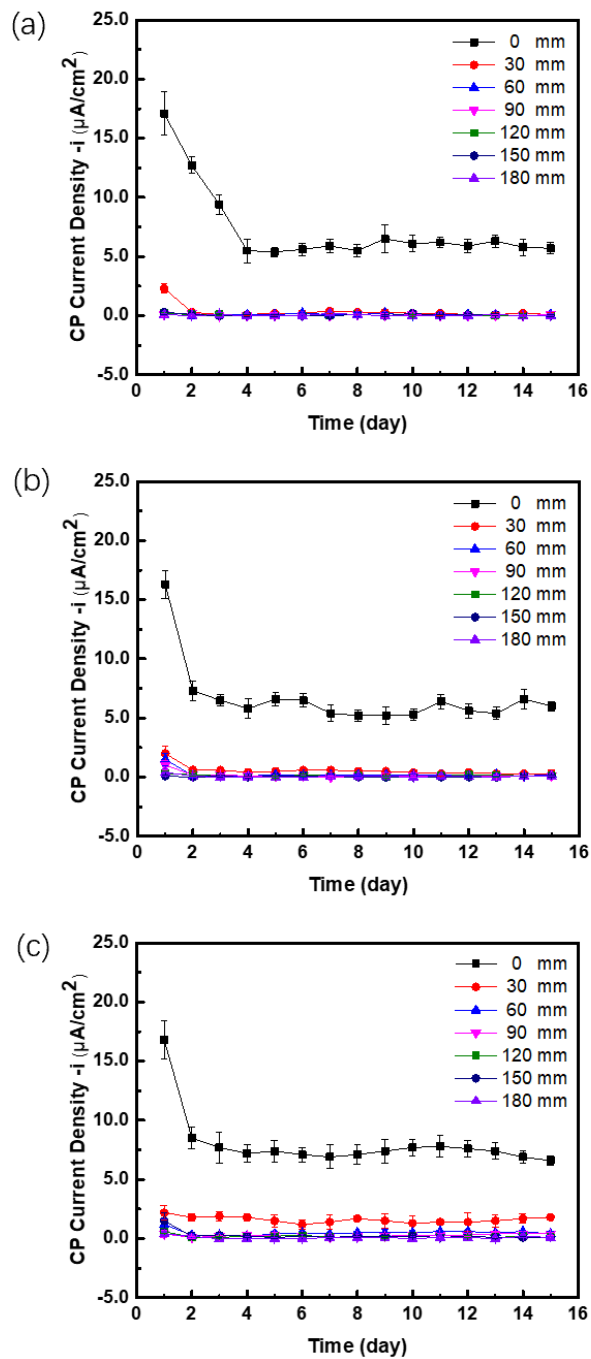


**Figure 3.15 Time dependence of cathodic current density of X52 steel under disbonded PE coating at varied disbonding depths from the open holiday (10 mm in diameter) with various disbonding thicknesses of (a) 120  $\mu\text{m}$ , (b) 240  $\mu\text{m}$  and (c) 360  $\mu\text{m}$  in the simulated soil solution, where a CP potential of -925 mV (CSE) is applied at the holiday.**

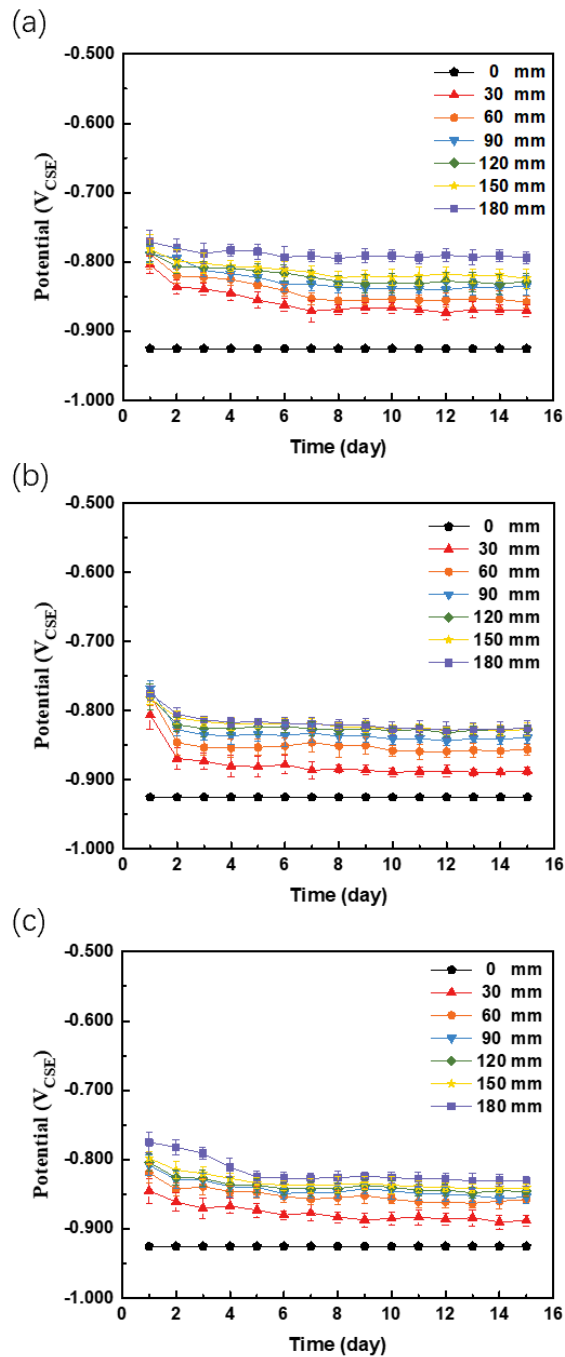


**Figure 3.16 Time dependence of the distribution of local potential under disbonded PE coating at varied disbonding depths from the open holiday (10 mm in diameter) with various disbonding thicknesses of (a) 120 μm, (b) 240 μm, and (c) 360 μm in the simulated soil solution, where a CP potential of -925 mV (CSE) is applied at the holiday.**

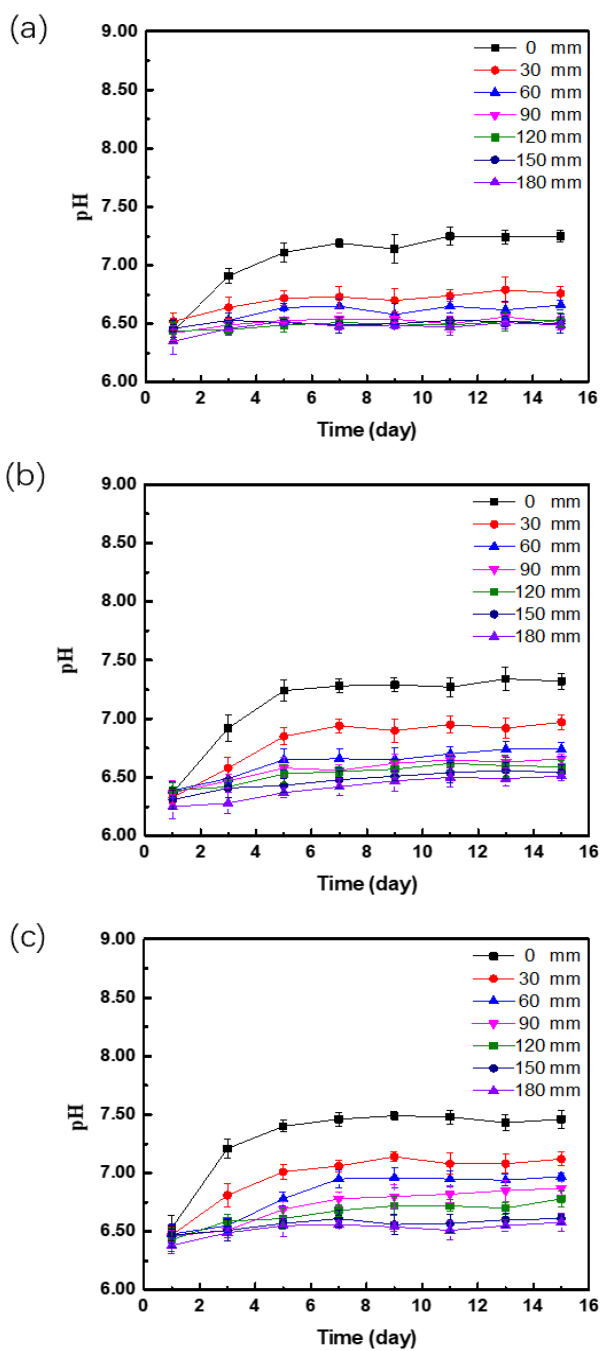


**Figure 3.17 Time dependence of the distribution of solution pH under disbonded PE coating at varied disbonding depths from the open defect (10 mm in diameter) with various disbonding thicknesses of (a) 120  $\mu\text{m}$ , (b) 240  $\mu\text{m}$  and (c) 360  $\mu\text{m}$  in the simulated soil solution, where a CP potential of -925 mV (CSE) is applied at the holiday.**

**Fig. 3.17** shows the time dependence of the distribution of solution pH under disbonded PE coating at varied disbonding depths from the open defect (10 mm in diameter) with various disbonding thicknesses in the simulated soil solution, where a CP potential of -925 mV (CSE) is applied at the holiday. It is seen that the solution pH tends to be the value of the originally prepared solution as the disbonding depth increase, indicating the CP permeability decreases with the increasing disbonding depth. At individual disbonding depths, the CP enhanced pH elevation tends to be more obvious with the increasing disbonding thickness, especially at the disbondment bottom. Therefore, the increasing disbonding thickness facilitate the CP permeability under coating disbondment.

### 3.4 Discussion

#### 3.4.1 Permeability of PE coating to CP

The permeability of the PE coating to CP current can be described by the ratio of the current density which passes through the coating to the required cathodic current density to protect the steel completely. This ratio is expressed by the equation below:

$$p = \frac{i_{CP}}{i_0} \times 100\% \quad (3.1)$$

where,  $p$  is the permeability of coating,  $i_{CP}$  is the CP current density at a certain CP potential, and  $i_0$  is the CP current density for complete cathodic protection at the same CP potential. The calculated permeability of PE coatings with different thickness is shown in **Table 3.2**. It is seen that the CP permeability of PE coating is quite low, indicating that almost all CP current can be

blocked by PE coating. And the coating thickness has little effect on the CP permeability of PE coating, as shown in **Table 3.2**. Therefore, PE coating is impermeable to CP current.

**Table 3.2 Permeability of PE coatings with different thickness at the CP potential of -925 mV(CSE).**

Thickness (mm)	$i_0$ ( $\mu\text{A}/\text{cm}^2$ )	$i_{CP}$ ( $\text{nA}/\text{cm}^2$ )	$p$
1.0		$-2.04 \times 10^{-2}$	0.00013%
1.5	-16.25	$-1.73 \times 10^{-2}$	0.00011%
2.0		$-1.61 \times 10^{-2}$	0.00010%

### 3.4.2 Effect of holiday size on CP permeability

The CP permeability of PE coating can be affected by the presence of holiday on coating. While the CP is applied, with the decrease of holiday size, the potential of steel under disbonded coatings with holiday tends to be less negative, which means the CP permeability reduce. For large holidays (holiday diameters are 10 and 4 mm), the potential of steel electrodes was close to applied CP potential, thus the steel electrodes are associated with an effective CP, no obvious corrosion phenomenon was found. However, for small holidays (holiday diameters are 2, 1 and 0.5 mm), the potential of electrode is much less negative than the applied CP potential, indicating that applied CP can be shielded partially or even completely. Therefore, although CP potential is applied, the steel electrodes can still experience corrosion. It is worth noting that, during the current density measurements on the steel electrodes, the time dependent current density showed different trends for large holiday and small holiday, as shown in **Fig. 3.9**. The large holiday allows enough high initial CP current density to penetrate in the first day, which

ensured adequate polarization. Then the subsequent CP current density shows a significant drop and then remains stable due to the formation of calcareous deposits (consisting primarily of calcium carbonate) on the steel surface under CP application. The applied CP enhances the water reduction reaction on cathode (steel surfaces), resulting in the generation of OH<sup>-</sup>. Then the hydroxyl formed at the steel surface reacts with bicarbonate ions present in soil solution to form carbonate ions (reaction 3.2) which, in turn, precipitate as insoluble calcium carbonate (reaction 3.3) on the surface of the steel [62]



The formed calcareous deposits can reduce the effective cathodic surface area (i.e. the polarization resistance is reduced) [63], thus the required CP current density decrease. For small holiday, as the holiday diameter is 2 mm, although the CP current density shows a similar trend to that at the large holiday, the penetrative initial CP current density is not enough to adequate polarization and form compact calcareous deposits on steel surface to prevent steel from corrosion, as evidenced by the optical image shown in **Fig. 3.8c**. This indicates that the CP current can be partially shielded by the 2mm-holiday. However, when the holiday is as small as 1mm and 0.5 mm in diameter, the CP current density was much lower than the required current density for complete cathodic protection, demonstrating the CP current can be shielded by the small holiday. Apparently, all results obtained support that the CP permeability of PE coating can be affected by the presence of holiday on coating.

### ***3.4.3 Effect of the disbonding geometry on CP permeability under PE coating disbondment***

The CP permeability under PE coating disbondment highly depends on the distance from the open holiday (i.e., the disbonding depth), as shown in **Figs. 3.15, 3.16 and 3.17**. The measurements of CP current show that the applied CP is blocked, at least partially, by the coating disbondment. With the increasing disbonding depth, the local potential from the holiday to the disbondment tends to be less negative, and the CP enhanced pH elevation becomes less obvious until the original solution pH is reached. This nonuniform distribution of CP current, local potential and solution pH from the open holiday toward the disbondment bottom indicates that the CP permeability tends to be reduced with the increasing disbonding depth. The surface characterization (**Figs. 3.12, 3.13 and 3.14**) shows that with the coating disbonding depth increases, the corrosion of steel increases and thicker corrosion scale is formed on the steel surface. This also demonstrates that the CP permeability decreases with the increasing distance from open holiday.

The CP permeability of coating disbondment is also affected by the coating disbonding thickness. The measurements of CP current density, local potential and solution pH under disbonded coating show that when the coating disbondment becomes wider (increase in disbonding thickness), the CP current density under disbonded coating increases slightly, the potential is closer to that at the open defect, and the CP enhanced pH elevation seems to be more obvious. This demonstrates that the CP shielding effect of disbonded coating tends to be mitigated as the coating disbondment becomes wider, indicating the CP permeability decreases with the disbonding thickness increases. The phenomenon is not only because of the blocking effect of coating disbondment on CP current but also due to the conductivity of the trapped solution under disbonded coating. Under narrow disbonding gaps, the CP permeability is further

reduced by limited diffusion of conductive ionic species through the thin solution layer trapped under the disbonded coating. Thus, although the full CP is applied on open holiday, the CP is still shielded either partially or completely at the disbonded area. With increasing disbonding thickness, the distribution of CP current diffusion can be increased around the defect. The increased solution volume under the wider coating disbondment also enhances the diffusion of species, facilitating the CP permeation into the coating disbondment.

In conclusion, the geometrical factors (i.e., disbonding depth and disbonding thickness) of the coating disbondment play an essential role in CP permeability under coating disbondment.

#### ***3.4.4 Corrosion Mechanism of cathodically protected pipelines under coating disbondment***

At large open holiday (holiday diameters are 10 and 4 mm), as the applied CP completely penetrate, the steel can be cathodic polarized and protective calcareous deposits will be formed on the steel surface. Under full CP, the anodic and cathodic reactions in deoxygenate near-neutral pH soil solution are primarily generation of oxygen and water reduction, respectively.

However, under the coating disbondment and PE coating membrane with small holiday (holiday diameters are 2, 1 and 0.5 mm), the CP is shielded completely or partially from reaching the steel and the steel may at its corrosion potential. Therefore, the anodic and cathodic reactions in deoxygenate near-neutral pH soil solution are primarily the iron oxidation and reduction of water, respectively. It is well known [64] that an iron carbonate scale would form on the steel surface during corrosion of the steel in the CO<sub>2</sub> containing environment. The structure and property of the scale affect the further CP permeability. With insufficient CP and immersing in the solution purging with 5%CO<sub>2</sub>/N<sub>2</sub>, the dissolution reaction of steel dominates the anodic

process under disbonded coating. When the concentration of  $\text{Fe}^{2+}$  reaches the saturation solubility of iron carbonate,  $\text{FeCO}_3$ , the scale would be formed by [65]:



Moreover, the scale would also be formed by a direct oxidation of steel [66]:



Therefore, the disbondment may become full of the  $\text{FeCO}_3$ , further increasing the blocking effect on CP permeability. Other's work confirmed the formation of  $\text{FeCO}_3$  scale on the steel surface at room temperature and atmospheric pressure. They found that the corrosion product scale consists of both the  $\text{FeCO}_3$  and  $\text{Fe}_3\text{C}$  [67].

Furthermore, the potential difference between the large open defect and the disbondment (specially the bottom) can produce separate anode and cathode sites. The cathodic reaction occurs at the open defect and the anodic reaction at the disbondment bottom. This is the main mechanism of localized corrosion on cathodically protected pipelines. Many field experiences demonstrate this phenomenon, extensive corrosion pits are found under disbonded coating on pipelines that are under CP [19].

### **3.5 Summary**

The disbonded defect-free PE coating is impermeable to CP current. Under the coating disbondment, the measured CP current density is too small to fully protect the steel electrode due to the significant blocking effect of the PE coating, therefore corrosion of steel specimens under the disbonded coatings still occur.

The geometrical factor of coating holiday plays an essential role in CP permeability of PE coating. With the increases in coating holiday size, the CP permeability of coating increases. For coating with holiday diameter larger than 4 mm, enough CP current can be penetrated through the holiday to protect the steel from corrosion attack.

Under the coating disbondment, the geometrical factor of the coating disbondment plays an essential role in CP permeability. With the increases of disbonding depth toward the disbondment bottom, the potential of the steel becomes positive and the solution pH decreases which is due to CP current diffusion can be shielded by coating disbondment and the formation of corrosion product. When the disbondment becomes wider, the CP shielding effect is mitigated.

## **Chapter Four: Microbiologically Influenced Corrosion of X52 Pipeline Steel in Thin Layers of Solution Containing Sulfate-Reducing Bacteria Trapped under Disbonded Coating**

### **4.1 Introduction**

Generally, underground pipelines are protected from corrosion by coating and CP. However, the protective measures are not always effective to protect the pipelines, especially when the coating is disbonded and the CP current is shielded from reaching the trapped electrolyte. As a result, corrosion can occur on pipelines under disbonded coating. The electrolyte trapped under disbonded coating usually has a low oxygen content [24], where the SRB growth is favored. Field investigations demonstrated that a higher number of SRB was counted at the corrosion sites under the disbonded coating than that in the bulk soil [21, 22]. At the same time, the electrolyte trapped under disbonded coating is usually thin, especially at the early stage of disbondment, where the steel corrosion experiences different processes as compared to that in the bulk solution [25]. It is thus expected that the MIC of pipeline steel occurring in a thin layer of electrolyte under coating would have different mechanisms and rates from that in a bulk solution.

Nowadays, the majority of investigations about MIC of pipeline steels in the presence of SRB are conducted in bulk solutions, which are not representative of the actual corrosive environment developed under the disbonded coating. Actually, there has so far been limited work to study the SRB induced pipeline corrosion under disbonded coating. For example, Xu et al. [49, 68] investigated the effect of SRB on crevice corrosion under disbonded coating in soil-extracted solutions, and found that the presence of SRB increased the energy consumption of CP system, which causes an alkalization of the solution in the crevice. Paula et al. [69] proposed that the biogenic sulfide led to formation of local galvanic cells and contributed to cathodic

depolarization. A review of the relevant research in the area shows that none of the available work characterizes the effect of the solution layer thickness on pipeline MIC under disbonded coating. As commented, corrosion, including MIC, of steels occurring in thin layers of solution would be different from that in bulk solutions. Without this knowledge, it is impossible to fully understand the mechanistic aspect of pipeline corrosion and MIC occurring under disbonded coating.

In this work, MIC of an X52 pipeline steel in thin layers of simulated soil solution in the presence of SRB under a disbonded PE coating was investigated by biological testing, weight-loss measurements, electrochemical measurements (i.e., electrochemical impedance spectroscopy, EIS, and potentiodynamic polarization), and surface characterization techniques (i.e., scanning electron microscopy, SEM, and energy-dispersive X-ray spectrum, EDS). As a comparison, tests and analysis were also conducted in sterile solutions. The effect of solution layer thickness on the steel corrosion was determined, and the mechanism of pipeline corrosion and MIC in thin layers of solution under coating was discussed.

## **4.2 Experimental**

### ***4.2.1 Material and solution***

Steel specimens used in this work were machined from an X52 steel pipe, with a chemical composition (wt.%): 0.24 C, 1.4 Mn, 0.45 Si, 0.025 P, 0.015 S, 0.10 V, 0.05 Nb, 0.04 Ti and Fe balance. The specimens used for electrochemical measurements were welded to copper wires, and sealed in epoxy resin, leaving a working area of 0.25 cm<sup>2</sup>. The specimen preparation was controlled carefully to ensure that bubbles and grooves were not generated at the steel/epoxy interface. The steel coupons used for weight-loss testing were machined into the dimension of 1

cm × 1 cm × 2 cm. All specimens were sequentially ground with #240, #400, #600, #800, and #1000 grit emery papers, cleaned with anhydrous alcohol and acetone, and dried in high-purity N<sub>2</sub> (99.999 %). The specimens were then sanitized by an ultraviolet (UV) lamp for 30 min.

In this work, the simulated soil solution was prepared based on the composition of the extracted soil solution in chapter three (**Table 3.1**), containing 0.0755 g/L NaHCO<sub>3</sub>, 0.0092 g/L NaCl, 0.0014 g/L NaNO<sub>3</sub>, 0.0773 g/L Na<sub>2</sub>SO<sub>4</sub>, 0.0619 g/L K<sub>2</sub>SO<sub>4</sub>, 1.116 g/L CaSO<sub>4</sub>·2H<sub>2</sub>O, 0.662 g/L MgSO<sub>4</sub>·7H<sub>2</sub>O. Before testing, the simulated soil solution was sterilized by autoclaving at 121 °C for 20 min, cooled in air to room temperature, and then deoxygenated by purging with high-purity N<sub>2</sub> until the content of dissolved oxygen in the solution was below 0.2 mg/L, as measured by a dissolved oxygen meter (ExStik DO600).

#### ***4.2.2 Experimental setup***

**Fig. 4.1a** shows the schematic diagram of the experimental setup of creation of a disbonded PE coating on the steel specimen, where a thin layer of solution trapped in the disbonding crevice. To prepare thin solution layers with varied thicknesses on the surface of the steel specimen, a PE membrane with a thickness of 1 mm was applied on the adhesion zone of the specimen surface using a double sided self-adhesive tape with various known thicknesses, i.e., 50, 150, 400 and 1000 μm. The boundaries of the steel/tape/coating system were sealed with epoxy. The gap thickness between the PE membrane and the steel specimen was determined by the thickness of the self-adhesive tape, and verified with a digital caliper and a coating thickness gauge (Fischer Technology, USA). The thickness of the created gap was defined as the thickness of the solution layer under the disbonded coating. In this work, four thicknesses of solution layers, i.e., 50, 150, 400 and 1000 μm, were created to investigate the MIC of X52 steel.

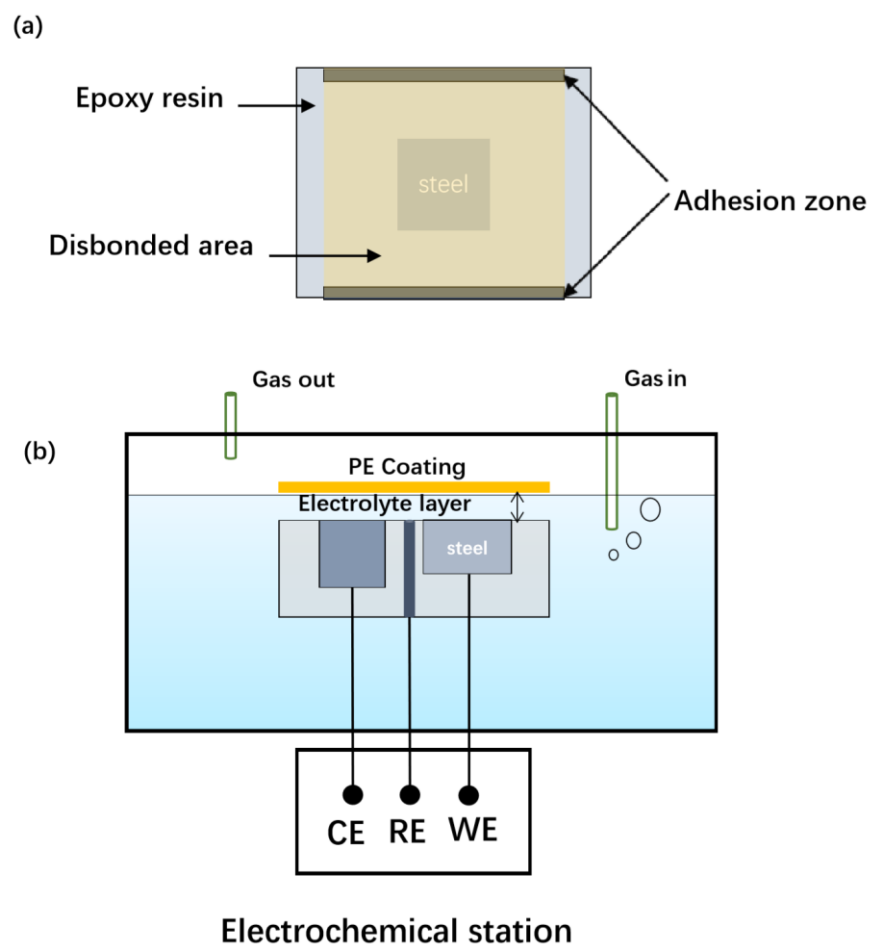


**Figure 4.1 Schematic diagrams of the experimental setup of (a) top view of creating a disbonded PE coating on the steel specimen, where a thin layer of solution trapped in the disbonding crevice, and (b) front view of electrochemical measurements in the thin solution layer trapped under disbonded coating, where WE, RE and CE refer to working, reference and counter electrodes, respectively.**

#### **4.2.3 Bacterial culturing and inoculation**

The SRB (ATCC 13541) used in this work were isolated from the soil samples. The culture medium for SRB contained 0.5 g/L  $K_2HPO_4$ , 0.5 g/L  $(NH_4)_2SO_4$ , 0.2 g/L  $(NH_4)_2Fe(SO_4)_2$ , 0.3

g/L MgCl<sub>2</sub>, 5.0 g/L sodium citrate, 1.0 g/L yeast extract and 3.5 g/L sodium lactate, with a pH of 7.2. Before inoculating, the culture medium was autoclaved at 121 °C for 20 min for sterilization, cooled in air to room temperature, and then purged with high-purity N<sub>2</sub> to remove oxygen until the content of dissolved oxygen was below 0.2 mg/L. After that, the SRB were incubated in the culture medium at 30 °C for 2 days. The 10 wt.% SRB-containing culture medium was added into the simulated soil solution in an anaerobic glove box to prepare the so-called test solution. The SRB cells attached on the steel specimen were enumerated by the most probable number (MPN) method according to ASTM Standard D 4412-15 [70], where the biofilm formed on the specimen surface was transferred into a phosphate-buffered saline (PBS) solution with a specific volume using a sterilized brush. The sessile SRB cells were enumerated using multiple dilutions. To ensure the accuracy of the results, three parallel samples were used for SRB cell counting under individual conditions.

#### ***4.2.4 Weight-loss measurements***

Prior to weight-loss measurements, the steel coupons were weighed by an electronic balance with an accuracy of 0.1 mg. The coupons were then immersed in the test solution in an anaerobic glove chamber. To ensure the reproducibility of the results, three parallel coupons were tested under each condition. The total testing time was 15 days, i.e., the period that was sufficient for SRB to achieve a stable growth and attachment on the steel specimen, as demonstrated in previous work [71]. After 15 days of testing, the coupons were removed from the test solution. The corrosion products formed on the coupon surface were removed carefully using a pickling solution containing imidazoline derivatives as corrosion inhibitor for 5 min. The coupons were then rinsed with distilled water immediately, and cleaned in absolute ethanol, dried by high-

purity N<sub>2</sub>, and weighed. The average corrosion rate (CR) of the steel (mm/year) was calculated by:

$$CR = \frac{8.76 \times 10^4 \times \Delta m}{\rho A t} \quad (4.1)$$

where  $\Delta m$  is weight-loss (g),  $\rho$  is density (g/cm<sup>3</sup>),  $A$  is coupon area (cm<sup>2</sup>), and  $t$  is time (h).

#### **4.2.5 Electrochemical measurements**

**Fig. 4.1b** shows schematically the experimental setup for electrochemical measurements on the steel specimen in a thin layer of solution under disbonded PE coating. Prior to testing, the test solution was purged with high-purity N<sub>2</sub>. The chamber was sealed to maintain the anaerobic environment. Electrochemical measurements were performed using a three-electrode cell through a Solartron Model 1280C electrochemical workstation. The steel specimen was used as working electrode (WE), a platinum plate as counter electrode (CE) and a saturate calomel electrode (SCE) as reference electrode (RE). The electrochemical measurements, including open-circuit potential (OCP), EIS and potentiodynamic polarization, were conducted to investigate the electrochemical corrosion activity, primarily uniform corrosion, of the steel under various testing conditions. The EIS and potentiodynamic polarization were measured after the OCP of the steel reached a steady value in the test solution at ambient temperature. The EIS was measured at the OCP, with a sinusoidal voltage signal of 10 mV in a frequency range from 2×10<sup>4</sup> to 10<sup>-2</sup> Hz. The potentiodynamic polarization curve was measured by potential-scanning from -250 to +350 mV

vs. OCP at a potential scan rate of 0.5 mV/s. To ensure reproducibility of the results, all tests were repeated at least three times.

#### ***4.2.6 Surface characterization***

After 15 days of immersion in the test solution under various conditions, the steel specimens were removed from the solution, and cleaned with the PBS solution (pH 7.2). The specimens were then dipped in the PBS solution containing 2.5% glutaraldehyde fixative for 8 h to immobilize sessile SRB cells [72]. After that, the specimens were dehydrated with various concentrations of ethanol solution (30%, 50%, 70%, 90% and 100%) for 10 min each successively, and dried using high-purity N<sub>2</sub>. Prior to SEM observation, a thin gold film with a thickness of 0.5 μm was coated on the specimen surface by a hummer sputter coater to improve the electrical conductivity. A field emission SEM (Field Electron and Ion Co. Quanta 250 FEG) and the coupled EDS (Bruker Quantax EDS) were used to characterize the morphology and elemental composition of the surface films formed on the steel specimen, respectively. After the SEM and EDS characterization, the surface film was removed following the same procedure as mentioned in weight-loss measurements. The morphology of the steel specimen without film was characterized by the field emission SEM.

### **4.3 Results and discussion**

#### ***4.3.1 Counts of sessile SRB cells on the specimen surface***

The sessile SRB cells attached on the steel specimen surface after 15 days of testing in the test solution with various thicknesses are shown in **Fig. 4.2**. For comparison, the SRB cell count measured in the bulk test solution is also included. It is seen that the number of sessile SRB cells

on the specimen surface increases with the increasing thickness of the solution layer. This indicates that the SRB grow better in thicker solution layers, and, as a result, there are more chances to attach to the specimen surface. Moreover, the increasing rate of the attached SRB cell number on the specimen decreases gradually with the solution layer thickness. For example, the sessile SRB cells increase from  $(4.0 \pm 2.5) \times 10^5$  cells/cm<sup>2</sup> to  $(5.7 \pm 3.6) \times 10^6$  cells/cm<sup>2</sup> when the solution layer thickens from 50 μm to 400 μm. When the solution layer is up to 1000 μm, the number of sessile SRB cells is  $(8.8 \pm 2.6) \times 10^6$  cells/cm<sup>2</sup>. It increases to  $(1.5 \pm 4.2) \times 10^7$  cells/cm<sup>2</sup> in the bulk solution. Thus, a decrease of the solution layer thickness is able to reduce the number of SRB cells attached on the steel specimen.

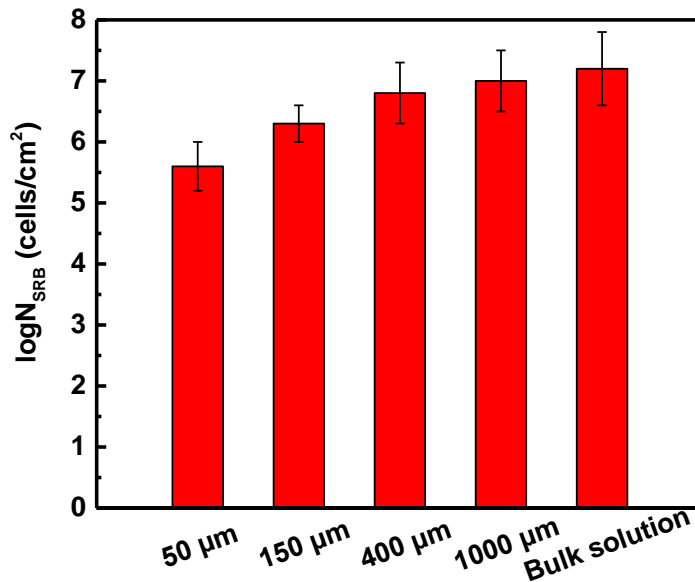


**Figure 4.2** The counts of sessile SRB cells (i.e.,  $N_{\text{SRB}}$ ) attached on the specimen surface after 15 days of testing in the test solution with various thicknesses.

### 4.3.2 Morphology of the surface films formed on the specimen

**Fig. 4.3** shows the SEM images of surface morphology of the steel specimens after 15 days of testing in the sterile solution layer of 50  $\mu\text{m}$  in thickness and the bulk solution, respectively. It is seen that there are some isolated corrosion products present on the specimen surface in the thin layer of solution. However, in the bulk solution, extensive corrosion products are generated on the specimen surface to form a layer of porous surface film. Obviously, the steel experiences increased corrosion in the bulk solution, as compared to the thin solution layer in the absence of SRB.

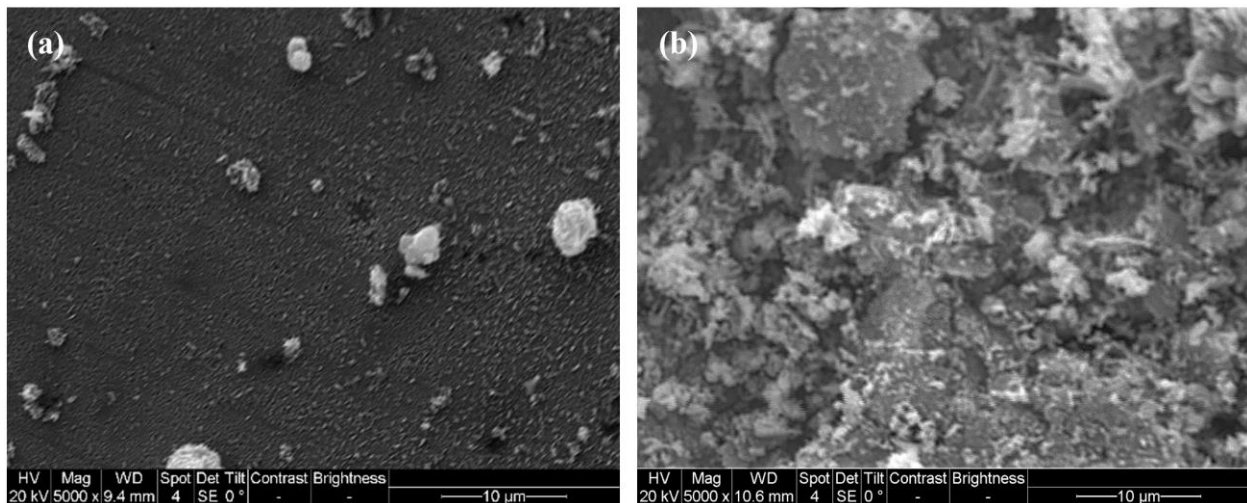


**Figure 4.3 SEM images of surface morphology of the steel specimens after 15 days of testing in (a) the sterile solution layer of 50  $\mu\text{m}$  in thickness and (b) the bulk solution, respectively.**

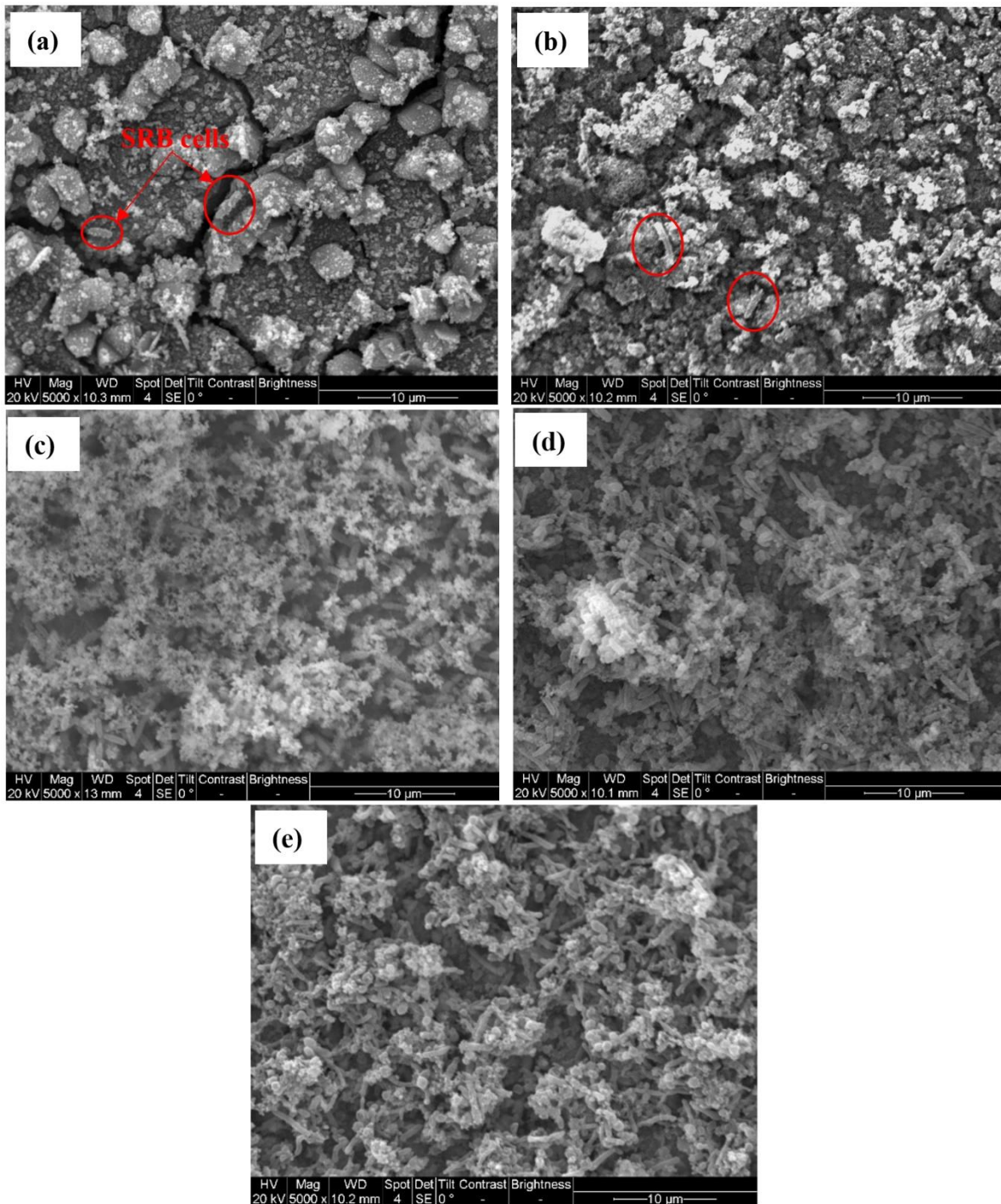


**Figure 4.4 SEM images of surface morphology of the steel specimen after 15 days of testing in the SRB-containing solution layers with various thicknesses (a) 50  $\mu\text{m}$ , (b) 150  $\mu\text{m}$ , (c) 400  $\mu\text{m}$ , (d) 1000  $\mu\text{m}$ , and (e) the bulk solution.**

**Fig. 4.4** shows the SEM images of surface morphology of the steel specimen after 15 days of testing in the SRB-containing solution layers with various thicknesses and the bulk test solution, respectively. In the thin layer of solution of 50  $\mu\text{m}$  in thickness, a layer of cracked surface film is formed on the specimen surface, and some isolated SRB cells are present, as shown in **Fig. 4.4a**. With the solution layer thickness increasing to 150  $\mu\text{m}$ , there are more corrosion products on the specimen surface than that in **Fig. 4.4a**. Although the surface film is still cracked, the cracks look smaller and shorter. SRB cells can be observed on the film too. With the further increase of the solution layer thickness to 400 and 1000  $\mu\text{m}$ , porous surface films cover the specimen extensively. More SRB cells overlap with the corrosion products (**Figs. 4.4c** and **4.4d**). There is no obvious difference in the morphology of the surface films formed in thick layers of solution (such as 400 and 1000  $\mu\text{m}$ ) from that in the bulk solution (**Fig. 4.4e**). The surface films include overlapped biofilm and corrosion products. As the solution layer thickness increases, there are more SRB cells present in the surface film. This result is consistent with the MPN counting results in **Fig. 4.2**. Moreover, compared to the surface film formed in the sterile solution with the layer thickness of 50  $\mu\text{m}$  (**Fig. 4.3a**), there are more corrosion products on the specimen surface in the presence of SRB (**Fig. 4.4a**), indicating the increased corrosion in the presence of SRB in the solution.

### ***4.3.3 Compositional characterization of the surface films***

**Tables 4.1** and **4.2** show the EDS results of the elemental composition of the surface films formed on the steel specimen after 15 days of testing under various solution layer thicknesses in the absence and presence of SRB in the simulated soil solution, respectively. In the absence of SRB, elements C and O are mainly from the corrosion products, i.e.,  $\text{Fe}(\text{OH})_2$  and  $\text{FeCO}_3$ ,

formed in the simulated soil solution [73]. In the thin layer of solution of 50  $\mu\text{m}$  in thickness, the high content of element Fe is from the steel substrate due to slight corrosion and isolated corrosion products present, as seen in **Fig. 4.2a**. The high content of O detected in the surface film formed in the bulk solution indicates more corrosion products are formed.

**Table 4.1 EDS results of the elemental composition of the surface films formed on the steel specimen after 15 days of testing under various solution layer thicknesses in the absence of SRB in the simulated soil solution.**

Solution		C	O	Fe	Si
50 $\mu\text{m}$ solution layer	At%	26.90	7.66	64.12	1.32
Bulk solution	At%	15.55	56.63	26.54	1.28

**Table 4.2 EDS results of the elemental composition of the surface films formed on the steel specimen after 15 days of testing under various solution layer thicknesses in the presence of SRB in the simulated soil solution.**

Solution layer thickness		C	O	Fe	S	P	Cl	Na	Mg	K	Ca
50 $\mu\text{m}$	At%	13.94	52.97	18.26	0.57	8.93	0.09	1.63	2.69	0.65	0.27
150 $\mu\text{m}$	At%	15.18	52.09	15.69	1.37	9.34	0.19	2.21	2.12	1.30	0.51
400 $\mu\text{m}$	At%	16.83	54.80	17.15	2.58	3.27	0.14	2.03	2.09	0.75	0.36
1000 $\mu\text{m}$	At%	21.96	46.05	15.51	7.29	3.63	0.33	2.23	2.55	0.28	0.17
Bulk	At%	22.84	45.31	13.89	8.04	3.84	0.36	2.56	2.26	0.78	0.12

In the presence of SRB, element S is detected on specimens tested in all solution layer thicknesses. Moreover, the content of S increases as the solution layer thickens. The S element contained in the surface films is from the metabolic sulfides generated by SRB. Element Fe is mainly from the corrosion products, especially for the surface films covering completely the steel substrate. The elements C and O are originated from corrosion products and the metabolic substances of SRB, such as extracellular polymeric substance (EPS) [52]. The content of element C increases with the increasing thickness of the solution layer. The element C is mainly from the EPS as the number of SRB cells increases remarkably as the solution layer thickness increases. When the thicknesses of the solution layer are 50 and 150  $\mu\text{m}$ , the detected elements P are much more than those obtained in other solution layer thicknesses. This may be attributed to the fact that the low content of sessile SRB cells on the specimen surface in thin layers of solution does not consume phosphorus, a required nutrient for SRB growth, at an appreciable level [74].

#### ***4.3.4 Weight-loss measurements***

**Fig. 4.5** shows the corrosion rate of the steel calculated from weight-loss measurements after 15 days of testing in the simulated soil solution with various thicknesses in the absence and presence of SRB, respectively. It is seen that, in the sterile solution, the corrosion rates of the steel in the 50  $\mu\text{m}$  solution layer and the bulk solution are  $0.05\pm 0.02$  and  $0.14\pm 0.04$  mm/y, respectively, while those obtained in the presence SRB under the identical condition are  $0.62\pm 0.04$  and  $0.66\pm 0.06$  mm/y, respectively. Obviously, the SRB contribute to accelerated corrosion of the steel in the solution. In the presence of SRB, with the increase of the solution layer thickness, the corrosion rate increases up to  $0.74\pm 0.13$  mm/y as the solution layer is 150  $\mu\text{m}$ , and then reduces to the smallest value of  $0.55\pm 0.05$  mm/y when the solution layer is 400

$\mu\text{m}$ . The corrosion rate then increases as the thickness of the solution layer increases up to the bulk solution. The results show that the steel corrosion in the thin layer of SRB-containing solution is highly dependent on the solution layer thickness.

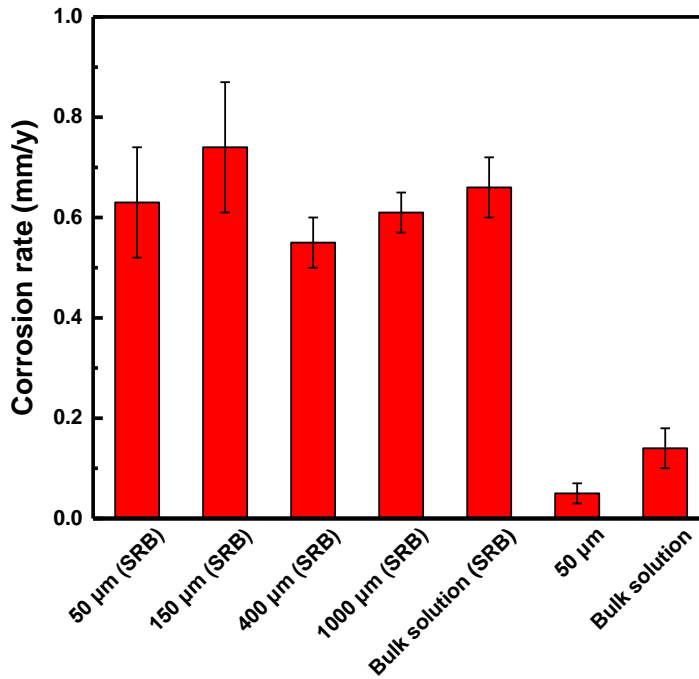
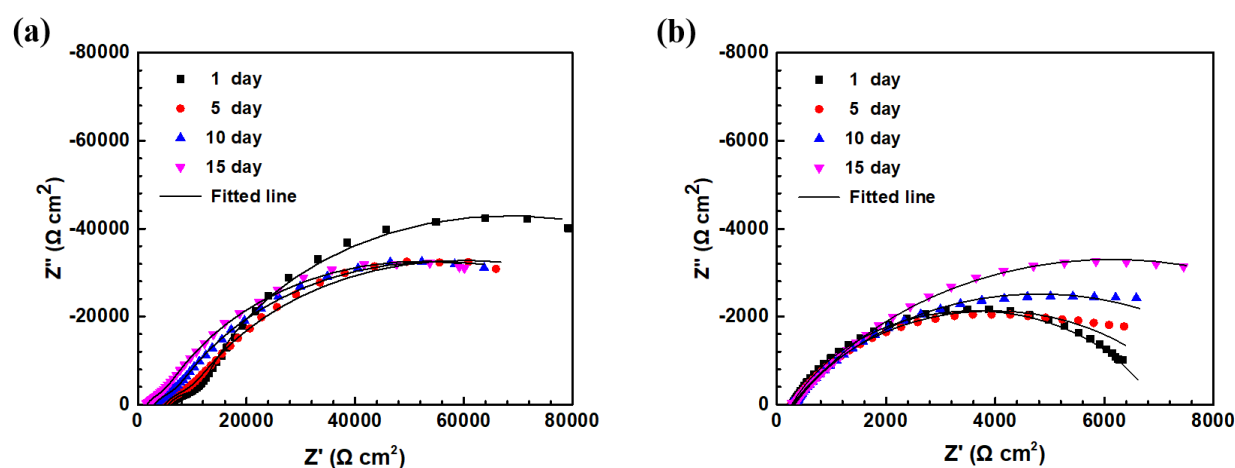


**Figure 4.5 Corrosion rate of the steel calculated from weight-loss measurements after 15 days of testing in the simulated soil solution with various thicknesses in the absence and presence of SRB, respectively.**

#### **4.3.5 Electrochemical measurements**

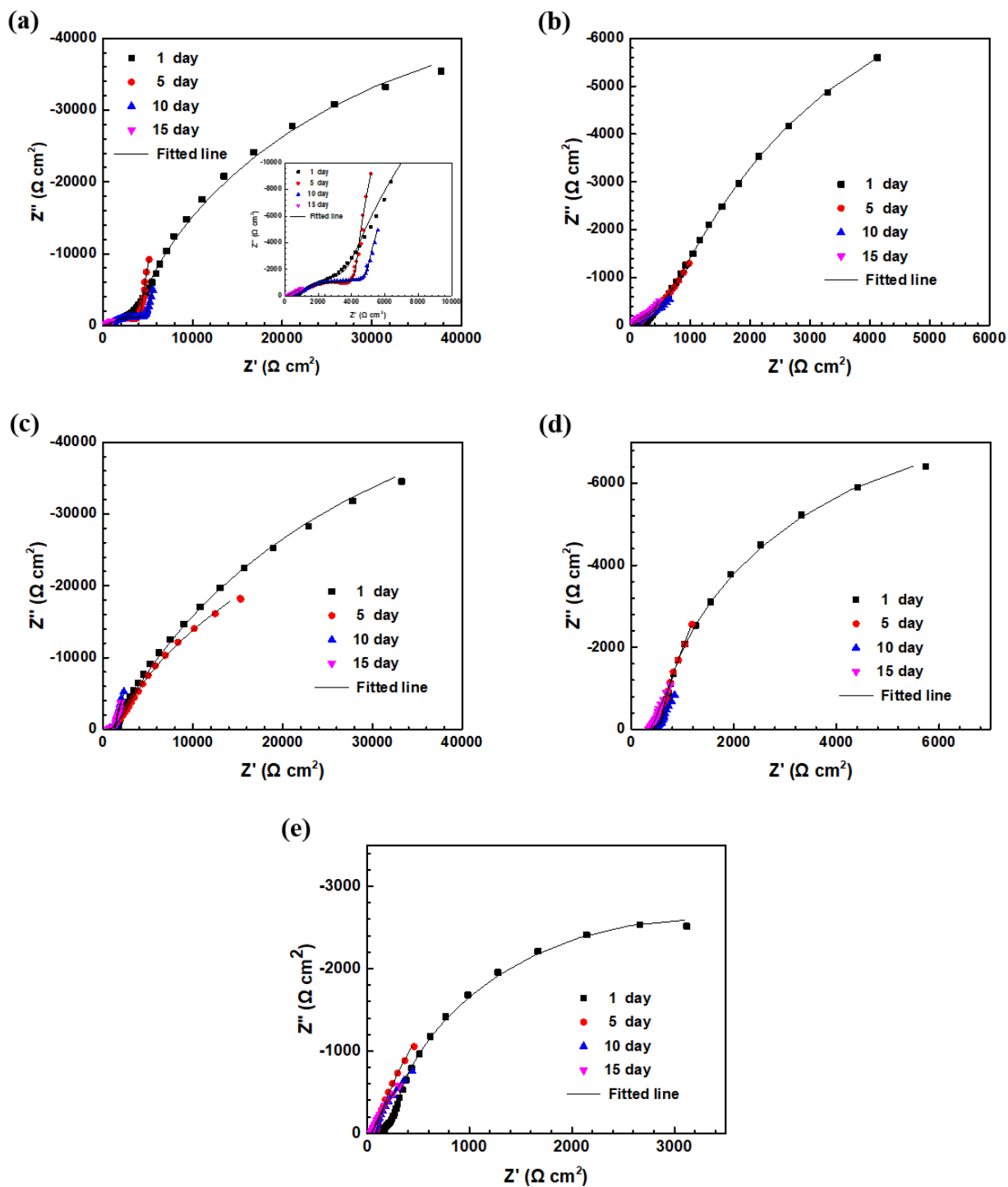
**Fig. 4.6** shows the Nyquist diagrams of the steel specimen measured in the 50  $\mu\text{m}$  solution layer and bulk solution in the absence of SRB as a function of time. It is seen in **Fig. 4.6a** that, in the thin solution layer, there is the largest semicircle at day 1, and the size of the semicircle decreases with time. However, the Nyquist diagrams measured in the sterile bulk solution feature differently, i.e., there is the smallest semicircle at day 1, and the size of the semicircle increases

with time. Moreover, at individual testing times, the size of the semicircle measured in the bulk solution is much smaller than that obtained in the thin solution layer (i.e., 50  $\mu\text{m}$  in thickness). Since the semicircle size is inversely proportional to corrosion rate of the steel, the results indicate that, in the sterile solution, the corrosion rate of the steel in bulk solution is higher than that in the thin solution layer, which is consistent with the weight-loss measurements in **Fig. 4.5**.



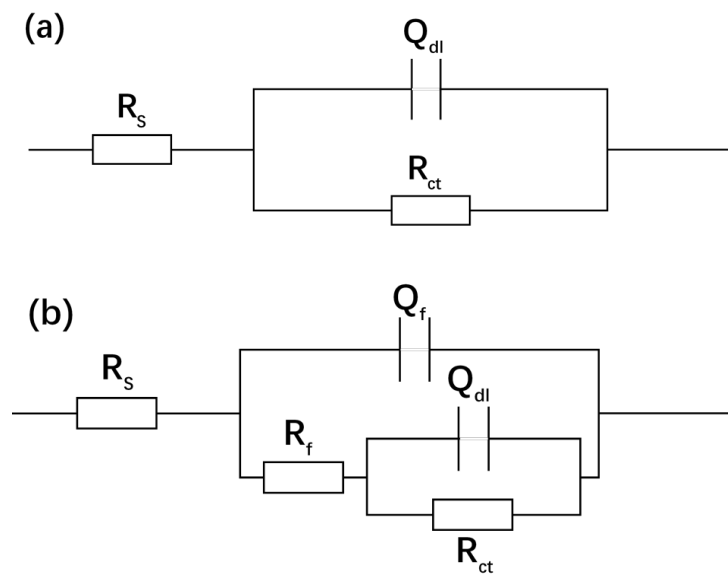
**Figure 4.6** Nyquist diagrams of the steel specimen measured in the (a) 50  $\mu\text{m}$  solution layer and (b) bulk solution in the absence of SRB as a function of time.

**Fig. 4.7** shows the Nyquist diagrams of the steel specimen measured in thin layers of solution with varied thicknesses and the bulk solution in the presence of SRB as a function of time. It is seen that, generally, the impedance plots measured at day one are featured of a big, incomplete semicircle. In the thin layers of solution, as the time increases, the initial semicircle is replaced with a small semicircle in the high frequency range and a straight line in the low frequency range. This indicates that the mass-transfer process is involved in the steel corrosion due to the formation of surface film on the steel surface.



**Figure 4.7 Nyquist diagrams of the steel specimen measured in thin layers of solution with varied thicknesses and the bulk solution in the presence of SRB as a function of time (a) 50  $\mu\text{m}$  (b) 150  $\mu\text{m}$  (c) 400  $\mu\text{m}$  (d) 1000  $\mu\text{m}$ , (e) bulk solution.**

In order to determine the dependence of the corrosion rate on the solution layer thickness, the measured impedance data are fitted with appropriate equivalent circuits are shown in **Fig. 4.8**, where  $R_s$  is solution resistance,  $R_f$  and  $Q_f$  are the resistance and constant-phase element of surface film, respectively,  $R_{ct}$  and  $Q_{dl}$  are charge-transfer resistance and the constant-phase element of the double-charge layer, respectively, and  $W$  is Warburg element representing the diffusion process influenced by surface film. Particularly, the circuit in **Fig. 4.8a** applies for the impedance plots obtained in the sterile bulk solution (i.e., **Fig. 4.6b**), where there is one time constant only. The circuit in **Fig. 4.8b** applies for those measured in the sterile solution layer of 50  $\mu\text{m}$  in thickness and in SRB-containing soil solution at day one, where two semicircles are obtained in the high and low frequency ranges, respectively. The circuit shown in **Fig. 4.8c** applies for the impedance data recorded in the SRB-containing bulk solution and the thin solution layers after day one, where a diffusive impedance is contained in the low frequency range. The fitting results are plotted as solid curves in **Figs. 4.6** and **4.7**, where the measured impedance data are fitted very well with the proper circuits, with a fitting error less than 10 %.



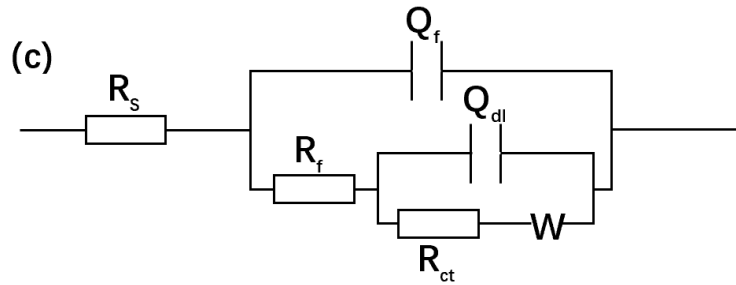


**Figure 4.8** Electrochemical equivalent circuits used to fit the EIS data measured in Figs. 4.6 and 4.7, where  $R_s$  is solution resistance,  $R_f$  and  $Q_f$  are the resistance and constant-phase element of surface film, respectively,  $R_{ct}$  and  $Q_{dl}$  are charge-transfer resistance and the constant-phase element of the double-charge layer, respectively, and  $W$  is Warburg element representing the diffusion process influenced by surface film.

Generally,  $R_p$ , the summation of  $R_f$  and  $R_{ct}$ , is inversely proportional to the corrosion rate of steels [75]. **Fig. 4.9** shows the time dependence of the fitted  $R_p$  values from the measured EIS data in **Figs. 4.6** and **4.7**. It is seen that, in the presence of SRB, the  $R_p$  values increase first, which is due to the formation of biofilm, and then drop with time, indicating the increased corrosion under the film. For the  $R_p$  values measured in the absence of SRB in **Fig. 4.9a**, the fluctuations are not as remarkable as those in **Fig. 4.9b**, showing that the corrosion product film formed on the steel surface is more stable. For the  $R_p$  obtained after 15 days of testing, there is the smallest value when the solution layer thickness is 150  $\mu\text{m}$ , indicating the largest corrosion rate at this condition. The result is well consistent with the weight-loss result in **Fig. 4.5**. Moreover, as the solution layer thickens from 400 to 1000  $\mu\text{m}$  and then the bulk solution, the  $R_p$  values decrease, which is also consistent with the increasing corrosion rate in **Fig. 4.5**.

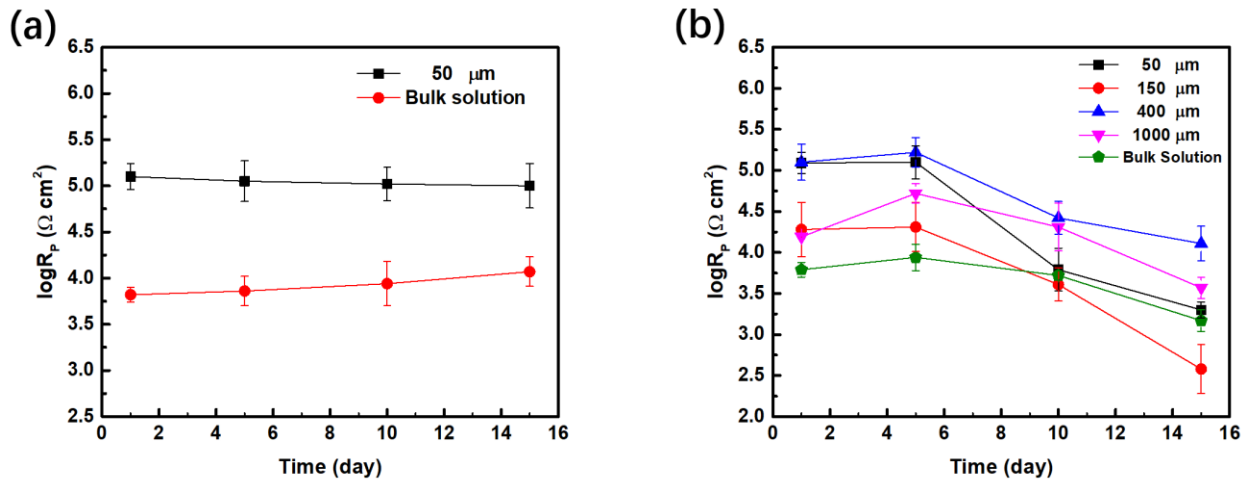


**Figure 4.9** Time dependence of the fitted  $R_p$  values from the measured EIS data in (a) Fig. 4.6 and (b) Fig. 4.7.

**Fig. 4.10** shows the potentiodynamic polarization curves of the steel specimen after 15 days of testing in thin layers of solution and bulk solution in the presence and absence of SRB, respectively. In the absence of SRB, both anodic and cathodic branches show activation-controlled polarization behavior in both the bulk solution and the thin solution layer. In the presence of SRB in the solution, a passive anodic behavior is observed in thin solution layers such as 50, 150 and 400  $\mu\text{m}$ . At individual anodic potentials, the passive current density increases when the solution layer thickens from 50 to 150  $\mu\text{m}$ , and then decreases at the thickness of 400  $\mu\text{m}$ . When the solution layer is as thick as 1000  $\mu\text{m}$ , the passive behavior is not observed, and the anodic curve shows an active polarization behavior, which is also observed in the bulk solution. It is found that, in thinner solution layers, the sessile SRB cells on the specimen surface are not sufficient in terms of activation of the generated corrosion products and biofilm, which usually possess somewhat protective ability to “passivate” the steel. As the

solution layer thickness increases, the number of SRB cells attached on the specimen increases, causing activation of the surface film, making it lose the protective ability to passivate the steel.

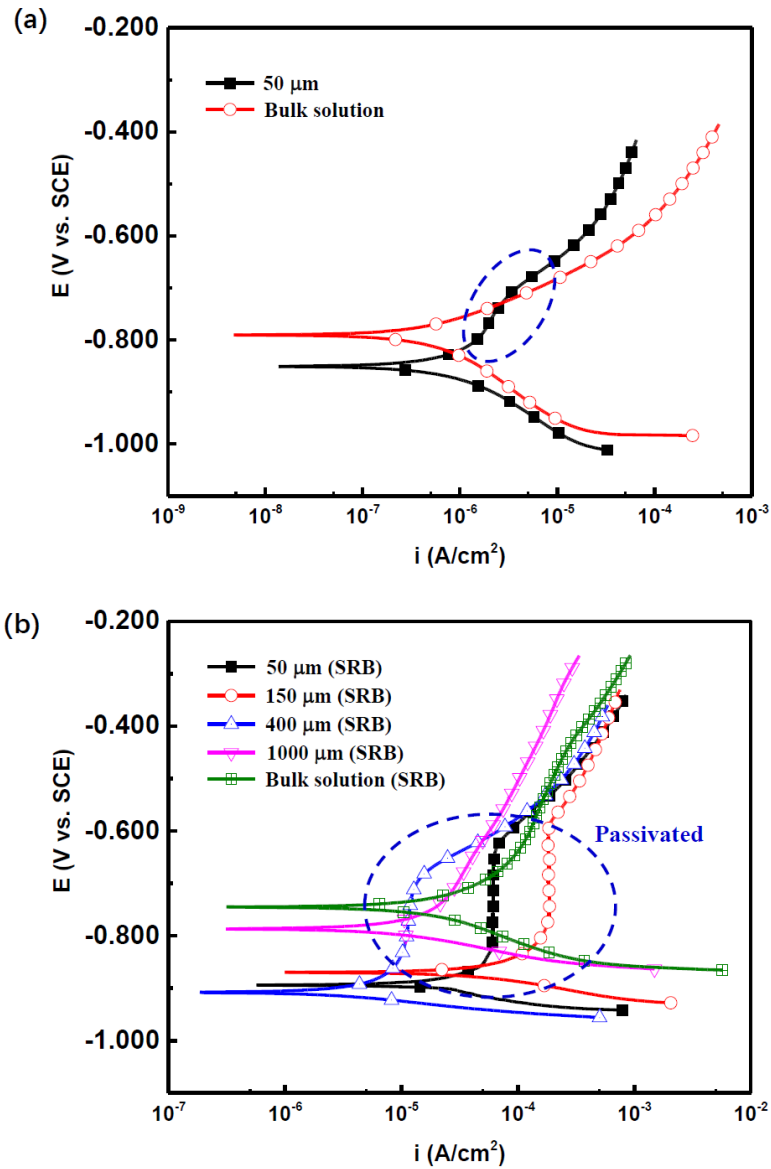


**Figure 4.10 Potentiodynamic polarization curves of the steel specimen after 15 days of testing in thin layers of solution and the bulk solution in the (a) presence and (b) absence of SRB, respectively.**

**Table 4.3** shows the fitted electrochemical corrosion parameters from the measured potentiodynamic polarization curves in **Fig. 4.10**. It is seen that, in the presence of SRB, the  $i_{\text{corr}}$  values obtained in the 50  $\mu\text{m}$  solution layer and the bulk solution are much higher than those in the absence of SRB under the identical testing condition, further confirming the accelerated corrosion of the steel by SRB. Moreover, the dependence of the  $i_{\text{corr}}$  values on the solution layer thickness in SRB-containing solution layers is well consistent with the results of the weight-loss measurements (**Fig. 4.5**) and the fitted  $R_p$  values from EIS data (**Fig. 4.9**).

**Table 4.3 Fitted electrochemical corrosion parameters from the measured potentiodynamic polarization curves in Fig. 4.10.**

	$b_a$ (V/dec)	$b_c$ (V/dec)	$E_{\text{corr}}$ (V vs. SCE)	$i_{\text{corr}}$ (A/cm <sup>2</sup> )
50 $\mu\text{m}$ + SRB	0.069	-0.030	-0.896	$1.48 \times 10^{-5}$
150 $\mu\text{m}$ + SRB	0.208	-0.040	-0.879	$6.91 \times 10^{-5}$
400 $\mu\text{m}$ + SRB	0.176	-0.024	-0.915	$4.14 \times 10^{-6}$
1000 $\mu\text{m}$ + SRB	0.334	-0.046	-0.799	$1.44 \times 10^{-5}$
Bulk solution + SRB	0.209	-0.085	-0.763	$2.64 \times 10^{-5}$
50 $\mu\text{m}$ , no SRB	0.290	-0.123	-0.854	$9.93 \times 10^{-7}$
Bulk solution, no SRB	0.090	-0.138	-0.791	$2.43 \times 10^{-6}$

#### 4.3.6 Corrosion morphology of the steel specimen upon removal of surface film

**Fig. 4.11** shows the SEM views of surface morphology of the steel specimens after 15 days of testing in the sterile 50  $\mu\text{m}$  solution layer and the bulk solution upon removal of the surface films. It is seen the steel does not corrode in the thin solution layer as much as that in the bulk

solution. There are some corrosion holes and signs in Fig. **4.11a**, while the corrosion is extensive on the specimen surface in Fig. **4.11b**.

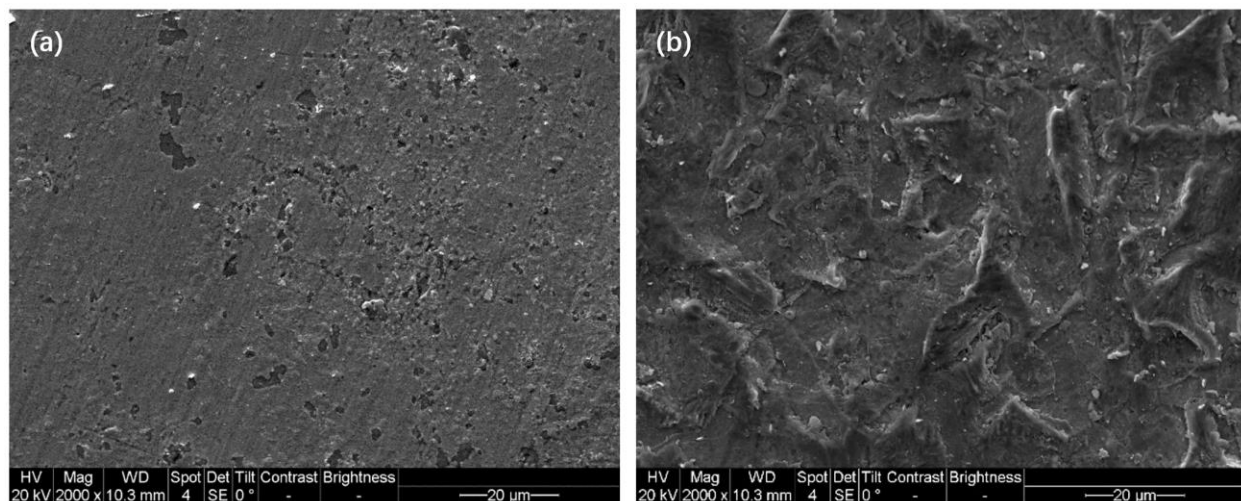


**Figure 4.11 SEM views of surface morphology of the steel specimens after 15 days of testing in the sterile (a) 50 µm solution layer and (b) the bulk solution upon removal of the surface films.**

The corrosion morphology of the steel specimen after 15 days of testing in thin layers of solution with varied thicknesses in the presence of SRB upon removal of the surface films is shown in **Fig. 4.12**. It is seen that extensive corrosion pits are present on the steel surface in the solution layer of 50 µm in thickness (**Fig. 4.12a**). With increasing solution layer thickness, pitting is not as obvious as that in **Fig. 4.12a**. The corrosion of the steel is mainly dominated by uniform corrosion. Morphologically, the difference of the corroded steel specimens is not obvious.

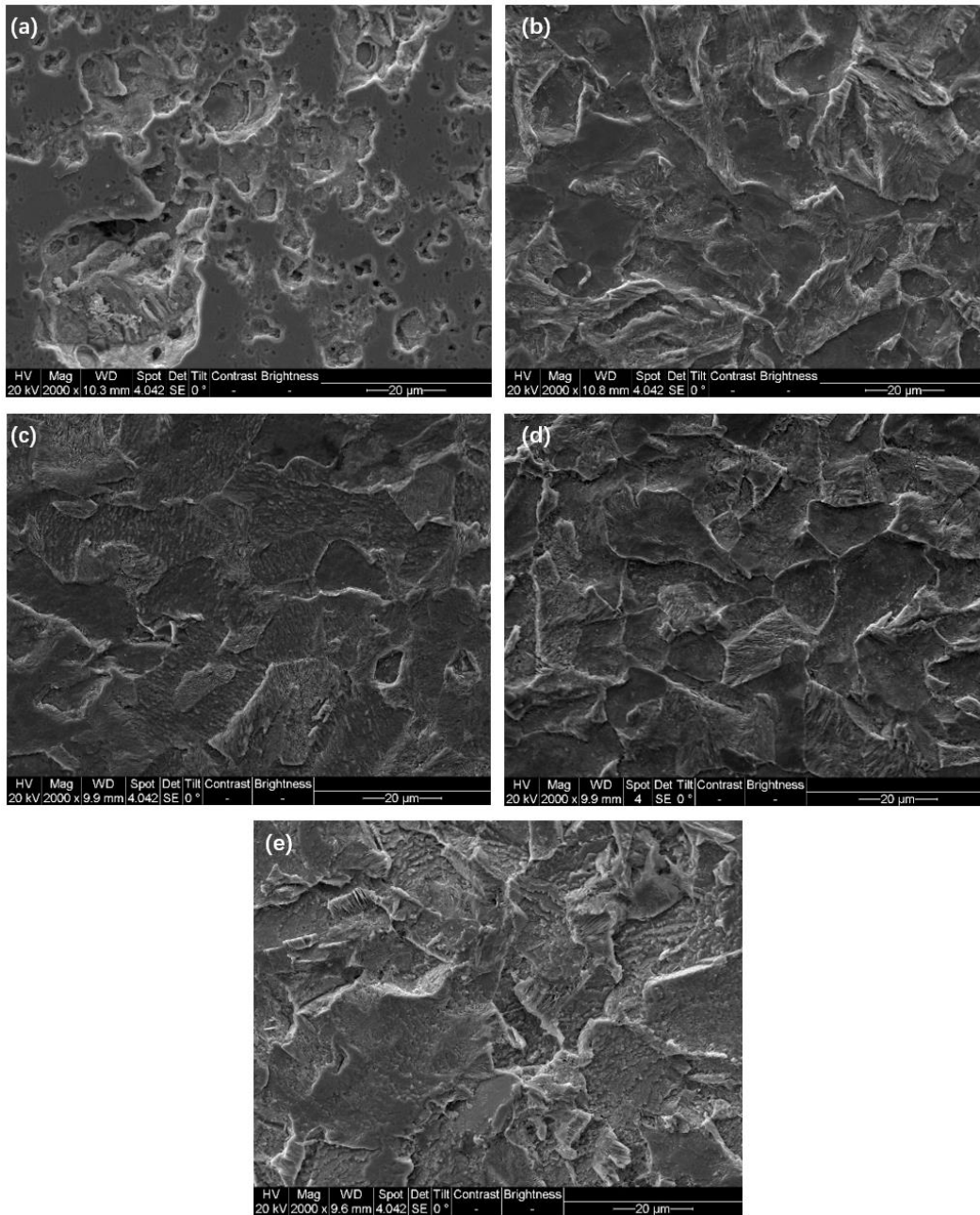
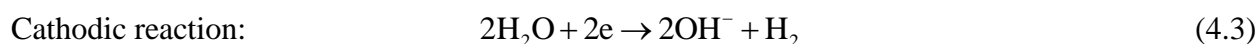


**Figure 4.12 Corrosion morphology of the steel specimen after 15 days of testing in thin layers of solution with varied thicknesses in the presence of SRB upon removal of the surface films (a) 50 μm, (b) 150 μm, (c) 400 μm, (d) 1000 μm, (e) bulk solution.**

#### ***4.3.7 Mechanistic aspects of pipeline corrosion and MIC in thin layers of sterile and SRB-containing simulated soil solutions trapped under coating***

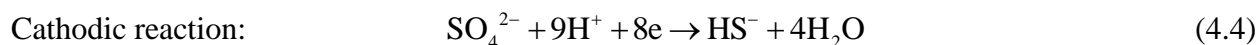
In anaerobic, near-neutral pH soil solutions, the anodic and cathodic reactions during pipeline corrosion include the oxidation of iron and the water reduction, respectively [76].



Generally, the corrosion process is very slow, leading to a small corrosion rate of the steels. As seen in **Fig. 4.5**, the average corrosion rate of X52 pipeline steel in the sterile bulk solution is about  $0.14 \pm 0.04$  mm/y. In a thin layer of solution trapped under disbonded coating, the corrosion of the steel occurs at an even smaller rate. This work finds that the corrosion rate is about  $0.05 \pm 0.02$  mm/y only when the solution layer is 50  $\mu\text{m}$  (**Fig. 4.5**). The polarization behavior in **Fig. 4.10a** shows that, compared to the active dissolution in the bulk solution, the steel shows a slightly “passivated” behavior between -0.80 V and -0.75 V (SCE), as marked, in the thin solution layer. This is attributed to the small volume of solution present on the steel surface, making it possible to form a layer of corrosion product deposit. The deposit layer formed in such a small volume of solution is usually more protective than the loose film formed in a bulk solution under the identical condition [77]. The results obtained from EIS measurements, including the fitted  $R_p$  (**Fig. 4.9**), and the electrochemical corrosion parameters fitted from the polarization measurements (**Table 4.3**) confirm the smaller corrosion rate of the steel in the thin solution layer than that in the bulk solution. The corrosion morphology of the

steel specimen also shows more extensive corrosion occurring on the steel in the bulk solution than in the thin solution layer (**Fig. 4.11**).

In the presence of SRB in the simulated soil solution, the steel corrosion is accelerated, leading to higher corrosion rates than those in the absence of SRB under identical testing conditions, as seen in **Fig. 4.5**. It is generally accepted that the SRB induced MIC of steels in anaerobic environments include the oxidation of the steel, i.e., reaction (4.2), and the reduction of sulfate ions [78]:



The rate of this reaction catalyzed by SRB is higher than that of the water reduction, i.e., reaction (4.3). The SRB growth is based on obtaining energy from either the reduction of sulfate ions, i.e., reaction (4.4), or organic matters and steels, which can be electron donors [24].

The present work demonstrates that the MIC of X52 pipeline steel under disbonded coating strongly depends on the thickness of the trapped solution layer. The weight-loss results show that there is the maximum corrosion rate when the solution layer thickness is 150  $\mu\text{m}$  (**Fig. 4.5**). The  $R_p$  values fitted from the impedance data (**Fig. 4.9**) and the  $i_{\text{corr}}$  fitted from the polarization measurements (**Table 4.3**) also give the smallest and the largest values, respectively, at the solution layer thickness of 150  $\mu\text{m}$ . Since all testing data are obtained from multiple tests on parallel specimens, it is believed that the critical thickness of the solution layer of 150  $\mu\text{m}$  under disbonded coating to achieve the largest corrosion rate is reliable, and it is also an interesting finding.

Pipeline steel corrosion in a thin layer of SRB-containing solution trapped under disbonded coating is resulted from synergism of SRB induced MIC of the steel and the film formation on the steel surface. This work proves that the counts of sessile SRB cells attached on the steel surface increase with the thickness of the solution layer present on the steel surface, indicating that thick solution layers favor the growth of SRB. This is mainly due to the fact that SRB cells grow well in a solution body due to the availability of nutrients. Moreover, the deposit of corrosion products in thin solution layers acts as a barrier to block the transport of nutrients to feed bacteria. The thicker solution layer contains more water, which is essential to the growth of SRB [77]. It is seen from this work that the number of sessile SRB cells on the steel surface increases approximately two orders of magnitude as the solution layer thickness increases from 50  $\mu\text{m}$  to the bulk solution. From the MIC viewpoint, the steel corrosion would increase with the increasing thickness of the trapped solution layer under coating.

At the same time, the mass-transfer of species to participate in corrosion reactions is limited by the film formed on the steel surface, as demonstrated by the presence of Warburg diffusive impedance in **Fig. 4.7**. In the solution layer as thin as 50  $\mu\text{m}$  in thickness, the surface film is dominated by corrosion products, such as  $\text{Fe}(\text{OH})_2$  and/or  $\text{FeS}$ , rather than biofilm due to the reduced number of SRB cells attached on the steel. The corrosion product film is not intact, containing many cracks (**Fig. 4.4a**), due to the limited solution volume for the solid deposition. The unfilmed steel would serve as the anode and the filmed part as the cathode, resulting in generation of a number of microcells for localized corrosion. As seen in **Fig. 4.12a**, there are many corrosion pits on the steel surface after removing the surface film. Although there are the fewest SRB cells on the specimen surface in the 50  $\mu\text{m}$  thick solution layer, the corrosion rate of

the steel is not the smallest. The key reason is that, in addition to uniform corrosion, localized pitting corrosion under cracked film occurs in the presence of SRB.

As the solution layer thickness increases to 150  $\mu\text{m}$ , the increased number of SRB cells would cause enhanced corrosion of the steel. However, the quantity of the SRB is still not sufficient to form a complete biofilm, and the formed surface film is dominated by corrosion products, as seen in **Fig. 4.4b**. Although not as cracked as the one in **Fig. 4.4a**, the film still contains small cracks, generating microcells to result in localized corrosion. Thus, corrosion pits are still visible on the specimen surface (**Fig. 4.12b**). Compared to corrosion occurring in the 50  $\mu\text{m}$  thick solution layer, the steel suffers from increased corrosion due to the increasing SRB cells and the occurrence of localized corrosion under cracked surface film when the solution layer is 150  $\mu\text{m}$  in thickness.

With the further increase of the solution layer thickness to 400  $\mu\text{m}$ , a layer of complete surface film containing both biofilm and corrosion products is formed on the steel surface, as seen in **Fig. 4.4c**. As the complete film possesses somewhat protective ability to the underlying steel, the corrosion rate of the steel reduces (**Fig. 4.5**). Although the number of SRB cells increases compared to the thinner solution layers (e.g., 50 and 150  $\mu\text{m}$ ), the biofilm overlapped with corrosion products would protect the steel. The uniform corrosion dominates the corrosion type, and localized pitting corrosion is not observed (**Fig. 4.12c**). With the increase of the solution layer to 1000  $\mu\text{m}$  and up to bulk solution, the surface film, which is mainly composed of overlapped biofilm and corrosion products, as seen in **Figs. 4.4d** and **4.4e**, does not alter morphologically compared to those in **Fig. 4.4c**. The increased corrosion rate is resulted from the increasing number of SRB cells on the steel surface.

#### 4.4 Summary

The number of sessile SRB cells attached on the steel surface increases with the thickness of the solution layer trapped under disbonded coating, indicating that the SRB grow better in thicker solutions layers, where there are more chances to attach to the steel surface. The corrosion rate of X52 pipeline steel depends on the thickness of the trapped solution layer under coating. The weight-loss testing, EIS and potentiodynamic polarization measurements demonstrate that, under the present testing condition, there exists a critical solution layer thickness of 150  $\mu\text{m}$ , where the largest corrosion rate of the steel is reached.

Pipeline corrosion in thin layers of solution containing SRB trapped under disbonded coating is resulted from synergism of SRB induced MIC and the film formation on the steel surface. In solution layers thinner than 150  $\mu\text{m}$ , such as 50  $\mu\text{m}$  in thickness, the number of sessile SRB cells on the steel is limited due to the blocking effect of the corrosion products depositing out of the small solution volume on mass-transfer of nutrients. However, localized pitting corrosion occurs under the cracked surface film which is mainly composed of corrosion products, rather than biofilm. When the solution layer is thicker than 150  $\mu\text{m}$ , such as 400  $\mu\text{m}$  in thickness, the increased SRB cell number makes the surface film composed of overlapped biofilm and corrosion products, which are extensively present on the steel surface to possess somewhat protective ability to decrease corrosion of the underlying steel. With the further increase in solution layer thickness and up to bulk solution, the surface film does not change obviously. The corrosion rate increases with the solution layer thickness due to the increasing number of SRB cells and thus, the MIC of the steel.

## Chapter Five: Conclusions and Recommendations

### 5.1 Conclusions

The disbonded defect-free PE coating is impermeable to CP current. Corrosion still occurs under coating disbondment even when the pipeline is under CP. When the coating contains defects such as holidays, the geometry of coating holiday plays an essential role in the CP permeability. With the increases in the coating holiday size, the CP permeability of coating increases. For coating with a holiday diameter larger than 4 mm, sufficient CP current can penetrate through the holiday to protect the steel from corrosion attack. Under the coating disbondment, the geometrical factor of the coating disbondment also plays an important role in CP permeability. With the increases of disbonding depth from open holiday, the potential of the steel becomes positive and the solution pH decreases which is due to the CP current diffusion can be shielded by coating disbondment and the formation of corrosion product. When the disbondment becomes wider, the CP shielding effect is mitigated.

In the presence of SRB, the number of sessile SRB cells attached on the steel surface increases with the thickness of the solution layer trapped under disbonded coating, indicating that the SRB grow better in thicker solutions layers, where there are more chances to attach to the steel surface. The corrosion rate of X52 pipeline steel depends on the thickness of the trapped solution layer under coating. Under the present testing condition, there exists a critical solution layer thickness of 150  $\mu\text{m}$ , where the largest corrosion rate of the steel is reached.

Pipeline corrosion in thin layers of solution containing SRB trapped under disbonded coating is resulted from synergism of SRB induced MIC and the film formation on the steel surface. In solution layers thinner than 150  $\mu\text{m}$ , the corrosion is mostly caused by localized pitting corrosion

occurs under the cracked surface which is mainly composed of corrosion products, rather than biofilm film. The number of sessile SRB cells on the steel is limited due to the blocking effect of the corrosion products depositing out of the small solution volume on mass-transfer of nutrients. However, as the solution layer is thicker than 150  $\mu\text{m}$ , the increased SRB cell number makes the surface film composed of overlapped biofilm and corrosion products, which are extensively present on the steel surface to possess somewhat protective ability to decrease corrosion of the underlying steel. With the further increase in solution layer thickness and up to bulk solution, the corrosion rate increases due to the increasing number of SRB cells and thus, the MIC of the steel.

## **5.2 Recommendations**

This research advances the understanding of the CP performance and the effect of solution layer thickness on pipeline MIC under PE coating disbondment. To apply the research results in practice, further work need to be conducted. In particular,

- 1) Based on the relevant results in this work, a modelling of CP permeability in various failure modes under coating disbondment could be built to guide the industry to evaluate or predicate the effectiveness of CP applied on pipelines.
- 2) While the mechanism of SRB-induced pipeline MIC under coating disbondment was studied in this work, further work can be devoted to the studies of pipeline MIC in multi-bacteria system, which simulates the real service environment in industry.

## References

- [1] National Energy Board (NEB) website: [www.neb-one.gc.ca](http://www.neb-one.gc.ca).
- [2] Canadian Energy Pipeline Association (CEPA) website: [www.cepa.com](http://www.cepa.com).
- [3] P. Gardoni, Risk and reliability analysis: Theory and applications, Springer, 2017.
- [4] H.A. Kishawy, H.A. Gabbar, Review of pipeline integrity management practices, International Journal of Pressure Vessels and Piping, 87 (2010) 373-380.
- [5] F. Cheng, Pipeline corrosion, Corrosion Engineering, Science and Technology, 50 (2015) 161-162.
- [6] M. Baker, Pipeline corrosion. Final report submitted to the US department of transportation pipeline and hazardous materials safety administration, Washington, DC, USA, (2008).
- [7] J. Byrd, Coatings and cathodic protection for pipeline: An introduction, Journal of Protective Coatings and Linings, 19 (2002) 50-56.
- [8] R. Norsworthy, J. Grillenberger, S. Brockhaus, EMAT, pipe coatings, corrosion control and CP shielding, Pipeline & Gas Journal, (2013).
- [9] D. Kuang, Y.F. Cheng, Study of cathodic protection shielding under coating disbondment on pipelines, Corrosion Science, 99 (2015) 249-257.
- [10] Y.Y. Zhang, W.L. Han, A.G. Li, H.Q. Shao, B.B. Xie, Study progress of cathodic protection current shielding of pipeline coatings, Corrosion and Protection, 31 (2010) 787-789+806.
- [11] L. Yan, M. Arafin, J.-P. Gravel, Penetration of cathodic protection into pipeline coating disbondment, in: CORROSION 2017, NACE International, 2017.
- [12] T. Jack, F. King, Y. Cheng, R. Worthingham, Permeable coatings and CP compatibility, in: 2002 4th International Pipeline Conference, American Society of Mechanical Engineers, 2002.
- [13] R. Norsworthy, Coatings used in conjunction with cathodic protection shielding vs non-

shielding pipeline coatings, CORROSION 2009.

[14] M. Roche, D. Melot, G. Paugam, Recent experience with pipeline coating failures, Journal of Protective Coatings and Linings, 23 (2006) 18.

[15] I. Thompson, J.R. Saithala, Review of pipeline coating systems from an operator's perspective, Corrosion Engineering, Science and Technology, 51 (2016) 118-135.

[16] G. Ruschau, Y. Chen, Determining the CP shielding behavior of pipeline coatings in the laboratory, in: CORROSION 2006, NACE International, 2006.

[17] M.M. Attar, M.M. Jalili, Evaluation of cathodic disbonding of three types of coatings by DC and AC methods, in: EUROCORR 2004 - European Corrosion Conference: Long Term Prediction and Modelling of Corrosion, 2004.

[18] I.C.P. Margarit, O.R. Mattos, J.R.R.M. Ferreira, J.P. Quintela, About coatings and cathodic protection: Electrochemical features of coatings used on pipelines, Journal of Coatings Technology, 73 (2001) 61-65.

[19] A.Q. Fu, Y.F. Cheng, Characterization of the permeability of a high performance composite coating to cathodic protection and its implications on pipeline integrity, Progress in Organic Coatings, 72 (2011) 423-428.

[20] G.R. Howell, Y.F. Cheng, Characterization of high performance composite coating for the northern pipeline application, Progress in Organic Coatings, 60 (2007) 148-152.

[21] P. Zhao, J. Yang, P. Zhu, C. Sun, J. Xu, A comparative study of the effects of sulfate reducing bacteria on corrosion of carbon steel Q235 under simulated disbonded coating with different width of aperture, in: Advanced Materials Research, 2012,.

[22] S.Y. Li, Y.G. Kim, K.S. Jeon, Y.T. Kho, Microbiologically influenced corrosion of underground pipelines under the disbonded coatings, Metals and Materials, 6 (2000) 281-286.

- [23] P. Zhao, J. Yang, D. Du, C. Sun, J. Xu, The effects of sulfate reducing bacteria on crevice corrosion behavior of Q235 steel, in: *Advanced Materials Research*, 2012.
- [24] D. Enning, J. Garrelfs, Corrosion of iron by sulfate-reducing bacteria: new views of an old problem, *Applied and Environmental Microbiology*, 80 (2014) 1226-1236.
- [25] A. Fu, Y. Cheng, Electrochemical polarization behavior of X70 steel in thin carbonate/bicarbonate solution layers trapped under a disbonded coating and its implication on pipeline SCC, *Corrosion Science*, 52 (2010) 2511-2518.
- [26] E.O. Obanijesu, V. Pareek, R. Gubner, M.O. Tade, Corrosion education as a tool for the survival of natural gas industry, *Nafta Sci. J.*, 61 (2010) 541-554.
- [27] H. Vanaei, A. Eslami, A. Egbewande, A review on pipeline corrosion, in-line inspection (ILI), and corrosion growth rate models, *International Journal of Pressure Vessels and Piping*, 149 (2017) 43-54.
- [28] Z. Ahmad, *Principles of corrosion engineering and corrosion control*, Elsevier, 2006.
- [29] L.L. Shreir, *Corrosion: corrosion control*, Newnes, 2013.
- [30] Y.F. Cheng, R. Norsworthy, *Pipeline Coatings*, NACE International, 2016.
- [31] V. Ashworth, 4.18 Principles of Cathodic Protection, *Shreir's Corros.*, (2010) 2747-2762.
- [32] T.I. Butler, Chapter 2 - PE Processes, in: J.R. Wagner (Ed.) *Multilayer Flexible Packaging*, William Andrew Publishing, Boston, 2010.
- [33] S.J. Thomas, *Pipeline Coatings Technology Review*, (2015).
- [34] A.L. Mamish, Tape coating system for pipeline corrosion protection, *PSTC Tech*, 32 (2013) 265-271.
- [35] M. Rahsepar, M. Asgharzadeh, M.J. Hadianfard, S.A.J. Jahromi, Failure analysis of disbondment of three-layer polyethylene coatings from the surface of buried steel pipelines,

Journal of Failure Analysis and Prevention, 15 (2015) 604-611.

[36] A. Samimi, S. Zarinabadi, An analysis of polyethylene coating corrosion in oil and gas pipelines, Journal of American science, USA, (2011).

[37] M.D. Holloway, Spend analysis and specification development using failure interpretation, CRC Press, 2011.

[38] F. Song, N. Sridhar, Chemistry and corrosion rates under pipeline disbonded coatings with or without cathodic protection, in: CORROSION 2007, NACE International, 2007.

[39] F. Song, D. Kirk, J. Graydon, D. Cormack, D. Wong, Corrosion under disbonded coatings having cathodic protection, Materials Performance, 42 (2003) 24-26.

[40] J. Perdomo, I. Song, Chemical and electrochemical conditions on steel under disbonded coatings: the effect of applied potential, solution resistivity, crevice thickness and holiday size, Corrosion Science, 42 (2000) 1389-1415.

[41] H. Wan, D. Song, X. Li, D. Zhang, J. Gao, C. Du, Failure mechanisms of the coating/metal interface in waterborne coatings: The effect of bonding, Materials, 10 (2017) 397.

[42] D. Kuang, Y.F. Cheng, Probing potential and solution pH under disbonded coating on pipelines, Materials Performance, 54 (2015) 40-45.

[43] X. Chen, X.G. Li, C.W. Du, Y.F. Cheng, Effect of cathodic protection on corrosion of pipeline steel under disbonded coating, Corrosion Science, 51 (2009) 2242-2245.

[44] D. Kuang, Y. Cheng, Effect of alternating current interference on coating disbondment and cathodic protection shielding on pipelines, Corrosion Engineering, Science and Technology, 50 (2015) 211-217.

[45] F. Varela, M.Y. Tan, M. Forsyth, A novel approach for monitoring pipeline corrosion under disbonded coatings, 2014.

- [46] F. Latino, F. Varela, M. Tan, M. Forsyth, An overview on cathodic shielding produced by disbonded coatings, AC Assosiation, Corrosion & Prevention 2016 Conference, Auckland, New Zealand, 2016.
- [47] K. Usher, A. Kaksonen, I. Cole, D. Marney, Critical review: microbially influenced corrosion of buried carbon steel pipes, *International Biodeterioration & Biodegradation*, 93 (2014) 84-106.
- [48] R. Newman, K. Rumash, B. Webster, The effect of pre-corrosion on the corrosion rate of steel in neutral solutions containing sulphide: relevance to microbially influenced corrosion, *Corrosion Science*, 33 (1992) 1877-1884.
- [49] J. Xu, K. Wang, C. Sun, F. Wang, X. Li, J. Yang, C. Yu, The effects of sulfate reducing bacteria on corrosion of carbon steel Q235 under simulated disbonded coating by using electrochemical impedance spectroscopy, *Corrosion Science*, 53 (2011) 1554-1562.
- [50] J. Xu, C. Sun, M. Yan, F. Wang, Variations of microenvironments with and without SRB for steel Q 235 under a simulated disbonded coating, *Industrial and Engineering Chemistry Research*, 52 (2013) 12838-12845.
- [51] X. Chen, G. Wang, F. Gao, Y. Wang, C. He, Effects of sulphate-reducing bacteria on crevice corrosion in X70 pipeline steel under disbonded coatings, *Corrosion Science*, 101 (2015) 1-11.
- [52] T. Liu, Y.F. Cheng, The influence of cathodic protection potential on the biofilm formation and corrosion behaviour of an X70 steel pipeline in sulfate reducing bacteria media, *Journal of Alloys and Compounds*, 729 (2017) 180-188.
- [53] F.M. Song, N. Sridhar, Modeling pipeline crevice corrosion under a disbonded coating with or without cathodic protection under transient and steady state conditions, *Corrosion Science*, 50 (2008) 70-83.

- [54] K.R. Larsen, Using pipeline coatings with cathodic protection: Protective coatings need to maintain integrity under operating environments and in the presence of CP, *Materials Performance*, 55 (2016) 32-35.
- [55] C. Dong, A. Fu, X. Li, Y. Cheng, Localized EIS characterization of corrosion of steel at coating defect under cathodic protection, *Electrochimica Acta*, 54 (2008) 628-633.
- [56] R. Norsworthy, S. Brockhaus, J. Grillenberger, M. Ginten, EMAT, pipe coatings, corrosion control and cathodic protection shielding, in: *CORROSION 2013*, NACE International, 2013.
- [57] D.-T. Chin, G. Sabde, Current distribution and electrochemical environment in a cathodically protected crevice, *Corrosion*, 55 (1999) 229-237.
- [58] A. Fu, Y. Cheng, Characterization of corrosion of X65 pipeline steel under disbonded coating by scanning Kelvin probe, *Corrosion Science*, 51 (2009) 914-920.
- [59] A. Eslami, R. Kania, B. Worthingham, G.V. Boven, R. Eadie, W. Chen, Corrosion of X-65 pipeline steel under a simulated cathodic protection shielding coating disbondment, *Corrosion*, 69 (2013) 1103-1110.
- [60] BSS, ISO 11048: 2002, Soil quality-determination of water-soluble and acid-soluble sulfate.
- [61] V.d.F.C. Lins, M.L.M. Ferreira, P.A. Saliba, Corrosion resistance of API X52 carbon steel in soil environment, *Journal of Materials Research and Technology*, 1 (2012) 161-166.
- [62] A. Bahadori, Prediction of scale formation in calcium carbonate aqueous phase for water treatment and distribution systems, *Water Quality Research Journal*, 45 (2010) 379-389.
- [63] C. Lee, R. Jacob, P. Morgan, R. Weatherhead, International experiences with cathodic protection of offshore pipelines and flowlines, TWI Report, (2007).
- [64] S. Nešić, Key issues related to modelling of internal corrosion of oil and gas pipelines—A review, *Corrosion Science*, 49 (2007) 4308-4338.

- [65] B. Linter, G. Burstein, Reactions of pipeline steels in carbon dioxide solutions, *Corrosion Science*, 41 (1999) 117-139.
- [66] G. Zhang, Y. Cheng, On the fundamentals of electrochemical corrosion of X65 steel in CO<sub>2</sub>-containing formation water in the presence of acetic acid in petroleum production, *Corrosion Science*, 51 (2009) 87-94.
- [67] G. Zhang, Y. Cheng, Electrochemical characterization and computational fluid dynamics simulation of flow-accelerated corrosion of X65 steel in a CO<sub>2</sub>-saturated oilfield formation water, *Corrosion Science*, 52 (2010) 2716-2724.
- [68] J. Xu, C. Sun, M. Yan, F. Wang, Corrosion of carbon steel Q235 in a crevice under a simulated disbanded coating, *Corrosion*, 70 (2014) 686-694.
- [69] M.S.d. Paula, M.M.M. Gonçalves, M.A.d.C. Rola, D.J. Maciel, L.F.d. Senna, D.C.B.d. Lago, Carbon steel corrosion induced by sulphate-reducing bacteria in artificial seawater: electrochemical and morphological characterizations, *Matéria (Rio de Janeiro)*, 21 (2016) 987-995.
- [70] ASTM D4412-15, Standard test methods for sulfate-reducing bacterial in water and water-formed deposits, (2015).
- [71] T. Liu, Y.F. Cheng, M. Sharma, G. Voordouw, Effect of fluid flow on biofilm formation and microbiologically influenced corrosion of pipelines in oilfield produced water, *Journal of Petroleum Science and Engineering*, 156 (2017) 451-459.
- [72] H. Liu, C. Fu, T. Gu, G. Zhang, Y. Lv, H. Wang, H. Liu, Corrosion behavior of carbon steel in the presence of sulfate reducing bacteria and iron oxidizing bacteria cultured in oilfield produced water, *Corrosion Science*, 100 (2015) 484-495.
- [73] B. Sherar, P. Keech, D. Shoesmith, Carbon steel corrosion under anaerobic-aerobic cycling

conditions in near-neutral pH saline solutions–Part 1: Long term corrosion behaviour, *Corrosion Science*, 53 (2011) 3636-3642.

[74] F. Rubio-Rincón, C. Lopez-Vazquez, L. Welles, T. van den Brand, B. Abbas, M. van Loosdrecht, D. Brdjanovic, Effects of electron acceptors on sulphate reduction activity in activated sludge processes, *Applied Microbiology and Biotechnology*, 101 (2017) 6229-6240.

[75] H. Liu, Y.F. Cheng, Mechanism of microbiologically influenced corrosion of X52 pipeline steel in a wet soil containing sulfate-reduced bacteria, *Electrochimica Acta*, 253 (2017) 368-378.

[76] Y.F. Cheng, *Stress corrosion cracking of pipelines*, John Wiley & Sons, 2013.

[77] R. Jiang, Y. Cheng, Mechanism of electrochemical corrosion of steel under water drop, *Electrochemistry Communications*, 35 (2013) 8-11.

[78] H. Liu, T. Gu, Y. Lv, M. Asif, F. Xiong, G. Zhang, H. Liu, Corrosion inhibition and anti-bacterial efficacy of benzalkonium chloride in artificial CO<sub>2</sub>-saturated oilfield produced water, *Corrosion Science*, 117 (2017) 24-34.